Mutation of a highly conserved isoleucine residue in loop 2 of several β-coronavirus macrodomains indicates that enhanced ADP-ribose binding is detrimental to infection

Catherine M. Kerr[1*], Jessica J. Pfannenstiel[1*], Yousef M. Alhammad[1], Joseph J. O'Connor[1], Roshan Ghimire[2], Rakshya Shrestha[2], Reem Khattabi[1], Pradtahna Saenjamsai[1], Srivatsan Parthasarathy[1], Peter R. McDonald[3], Philip Gao[4], David K. Johnson[5], Sunil More[3, 6], Anuradha Roy[3], Rudragouda Channappanavar[2, 6], Anthony R. Fehr[1#]

[1]Department of Molecular Biosciences, University of Kansas, Lawrence, Kansas 66045, USA
[2]Department of Veterinary Pathobiology, Oklahoma State University, Stillwater, Oklahoma 74078, USA
[3]High Throughput Screening Laboratory, University of Kansas, Lawrence, Kansas 66047, USA
[4]Protein Production Group, University of Kansas, Lawrence, Kansas 66047, USA
[5]Molecular Graphics and Modeling Laboratory and the Computational Chemical Biology Core, University of Kansas, Lawrence, Kansas 66047, USA
[6]Oklahoma Center for Respiratory and Infectious Diseases, College of Veterinary Medicine, Stillwater, Oklahoma 74078, USA

[*]These authors contributed equally to this work. Author order was determined by relative contributions to writing the manuscript.

[#]Correspondence: arfehr@ku.edu; Tel.: +1-(785) 864-6626 (K.S.)

Running title: Increased Mac1 ADP-ribose binding attenuates CoV infection

Keywords: coronavirus, MERS-CoV, SARS-CoV-2, MHV, non-structural protein 3, macrodomain, ADP-ribosylation, ADP-ribosylhydrolase, interferon

ABSTRACT

All coronaviruses (CoVs) encode for a conserved macrodomain (Mac1) located in nonstructural protein 3 (nsp3). Mac1 is an ADP-ribosylhydrolase that binds and hydrolyzes mono-ADP-ribose from target proteins. Previous work has shown that Mac1 is important for virus replication and pathogenesis. Within Mac1, there are several regions that are highly conserved across CoVs, including the GIF (glycine-isoleucine-phenylalanine) motif. To determine how the biochemical activities of these residues impact CoV replication, the isoleucine and the phenylalanine residues were mutated to alanine (I-A/F-A) in both recombinant Mac1 proteins and recombinant CoVs, including murine hepatitis virus (MHV), Middle East respiratory syndrome coronavirus (MERS-CoV), and severe acute respiratory syndrome coronavirus 2 (SARS-CoV-2). The F-A mutant proteins had ADP-ribose binding and/or hydrolysis defects that led to attenuated replication and pathogenesis in cell culture and mice. In contrast, the I-A mutations had normal enzyme activity and enhanced ADP-ribose binding. Despite increased ADP-ribose binding, I-A mutant MERS-CoV and SARS-CoV-2 were highly attenuated in both cell culture and mice, indicating that this isoleucine residue acts as a gate that controls ADP-ribose binding for efficient virus replication. These results highlight the function of this highly conserved residue and provide unique insight into how macrodomains control ADP-ribose binding and hydrolysis to promote viral replication.

AUTHOR SUMMARY

The conserved CoV macrodomain (Mac1) counters the activity of host ADP-ribosyltransferases by removing ADP-ribose from target proteins and is critical for CoV replication and pathogenesis. Mac1 is a potential therapeutic target for CoV disease and several groups are actively developing Mac1 inhibitors. However, we lack a basic knowledge of how many of the key residues in the Mac1 ADP-ribose binding pocket contribute to its biochemical and virological functions. In this study, we engineered alanine mutations into two highly conserved residues in the ADP-ribose binding pocket of Mac1, both as recombinant proteins and recombinant viruses for both MERS-CoV and SARS-CoV-2 to determine their importance in both Mac1 biochemical functions and CoV infection. Interestingly, an isoleucine-to-alanine mutation in loop 2 of both MERS-CoV and SARS-CoV-2 Mac1 proteins enhanced ADP-ribose binding. But surprisingly, that proved to be detrimental to virus infection, indicating that this isoleucine functions to control Mac1 ADP-ribose binding and is beneficial for virus replication and pathogenesis. These results provide unique insight into how macrodomains control ADP-ribose binding to promote infection and will be critical for the development of novel inhibitors targeting Mac1 that could be used to treat CoV-induced disease.

62 **INTRODUCTION**

63 Coronaviruses (CoVs), from the family *Coronaviridae* of the order *Nidovirales*, are large
64 positive-sense RNA viruses of both human and veterinary significance. In the past few decades,
65 there have been three significant outbreaks of lethal human CoV disease. The first outbreak
66 occurred in 2002-2003 when severe acute respiratory syndrome (SARS-CoV) emerged in China.
67 In 2012, Middle East respiratory syndrome (MERS)-CoV was reported in Saudi Arabia. More
68 recently, in late 2019, the SARS-CoV-2 emerged in Wuhan, China and rapidly spread around the
69 world, becoming the first CoV to be the cause of a pandemic (1).

70 CoVs genomes range in size from 26-32 kb and encode for four conserved structural
71 proteins, up to ten accessory proteins, and 15-16 non-structural proteins (nsps) that are expressed
72 in two polyproteins, polyprotein 1 a (pp1a) and polyprotein 1 ab (pp1ab). These polyproteins are
73 further cleaved by viral proteases into individual non-structural proteins. The nsps encode for a
74 variety of proteins that are necessary for replication and innate immune evasion, such as the RNA-
75 dependent RNA polymerase, main protease, helicase, N-7 methyltransferase, exoribonuclease, an
76 endoribonuclease, and many others. The largest of the CoV nsps is nsp3, which encodes for
77 multiple modular domains, including ubiquitin-like domains, nucleic acid binding domains, one
78 or two papain-like protease domains, a deubiquitinase domain, a CoV-Y domain, and one or more
79 macrodomains (2, 3). Nsp3 is also required for double-membrane vesicle (DMV) formation and
80 forms a pore within DMVs in the replication-transcription complex (RTC). Several domains of
81 nsp3 are required to form the pore within the RTC, including those from Ubl2 to the C-terminus
82 of nsp3 (4, 5).

83 Some CoVs encode for as many as 3 tandem macrodomains, termed Mac1, Mac2, and
84 Mac3. Mac1 is a conserved domain found in all CoVs, Togaviruses, Rubiviruses, and Hepatitis E

85 virus (6). The highly conserved structure of Mac1 consists of several central β-sheets surrounded
86 by 3 α-helices on each side (7-11). Mac1 has been shown to reverse ADP-ribosylation of proteins
87 *in vitro* (12-17). ADP-ribosylation is a common posttranslational modification that is catalyzed by
88 ADP-ribosyltransferases (ARTs) that utilize NAD^+ to covalently attach a single ADP-ribose unit,
89 mono-ADP-ribosylation (MARylaytion/MAR), or a chain of several ADP-ribose units, poly-ADP-
90 ribosylation (PARylation/PAR) to a target protein or nucleic acid (18, 19). These modifications are
91 crucial for cellular stress responses, including viral infections (20). The most common mammalian
92 ARTs are PARPs, and the most well studied PARP is PARP1, which is a target of anti-cancer drugs
93 due to its role in the DNA damage response. However, most PARPs are mono-ADP-
94 ribosyltransferases, many of which are IFN-stimulated genes (ISGs) and are known to impact virus
95 infections (21).

96 Several studies have demonstrated that the conserved macrodomain is critical for CoV,
97 alphavirus, and Hepatitis E virus infection, using either deletion or point mutations of the
98 conserved macrodomain (12, 22-30), indicating that these viruses are especially sensitive to host
99 PARP-mediated antiviral functions. However, despite clear evidence that Mac1 is critical for CoV
100 infection, there have only been a few studies that have investigated how individual residues
101 contribute to the biochemical functions of Mac1 and how those biochemical activities correlate
102 with CoV replication and pathogenesis. Initial studies of Mac1 in CoVs focused on the mutation
103 of a highly conserved asparagine residue to alanine or aspartic acid. This mutation largely impairs
104 Mac1 deMARylating activity, as has been demonstrated for the α-CoV 229E, and the β-CoVs
105 SARS-CoV, and SARS-CoV-2 proteins (9, 12, 29, 31). In most cases, these mutations did not
106 significantly reduce virus replication in cell culture but did lead to highly attenuated viruses in
107 mice (12, 25, 26, 29, 31). We also showed that the Asn-to-Ala mutation in the β-CoV murine

108 hepatitis virus strain JHM (MHV) led to poor replication in primary bone-marrow-derived
109 macrophages, which was reversed upon either knockdown or knockout of PARP12, demonstrating
110 that Mac1 specifically counters PARP activity (32, 33). Additionally, the Asn-to-Ala mutation in
111 MHV and SARS-CoV, as well as a complete Mac1 deletion and an Asn-to-Asp mutation in SARS-
112 CoV-2, lead to increases in IFN production following infection (12, 24, 29, 32). This function was
113 independent of its effect on virus replication, as the MHV Asn-to-Ala virus remained attenuated
114 in MAVS$^{-/-}$ cells and mice (32). This increase in IFN production following an MHV Mac1 mutation
115 infection, specifically the N1347A infection, is due to its ability to counter PARP activity, as PARP
116 inhibitors abolish this response (32). In addition, virus with the same mutation in SARS-CoV-2
117 (N1062A), as well as a complete Mac1 deletion virus, was more sensitive to IFNγ treatment in cell
118 culture and was attenuated *in vivo* when compared to WT virus (24). Furthermore, overexpression
119 of SARS-CoV-2 WT Mac1, but not the Asn-to-Ala mutation, reverses PARP14/PARP9/DTX3L
120 mediated ADP-ribosylation following IFNγ or poly(I:C) treatment (Hoch/Ahel papers) (16). The
121 only other mutations that have been evaluated both in the context of biochemical activity and virus
122 replication are D1022A, H1045A, and G1130V (all numbers based on the SARS-CoV Mac1) (12,
123 31). In the context of SARS-CoV, each of these mutations had reduced ADP-ribosylhydrolase
124 activity, replicated normally in cell culture, and were attenuated in mice (12). A later study
125 evaluated the role of the D1329A and G1439V mutations in MHV. Recombinant viruses with those
126 mutations, which are predicted to dramatically reduce Mac1 ADP-ribose binding, were highly
127 attenuated in cell culture, much more so than the aforementioned N1347A mutation (34). These
128 results indicate that ADP-ribose binding may be more critical for MHV than for SARS-CoV.
129 Additional evidence supporting this hypothesis was obtained from SARS-CoV-2, as the

130 orthologous D1044A mutation did not display increased sensitivity to IFNγ and was only partially
131 attenuated in mice (24).

132 The highly conserved isoleucine and phenylalanine residues in loop 2 are also of great
133 interest due to their conservation and positioning within the ADP-ribose binding pocket (Fig. 1A-
134 B) (7, 9, 11), though the impact of these residues on CoV replication has not been addressed. The
135 isoleucine appears to interact with the final glycine in loop 1 to form a narrow channel around the
136 diphosphate within the ADP-ribose binding domain that could be important for both binding and
137 hydrolysis. In contrast, the phenylalanine residue makes van der Waals interactions with the distal
138 ribose and orients the distal ribose for hydrolysis. In prior studies, mutation of phenylalanine-to-
139 leucine reduced enzyme activity of SARS-CoV-2 Mac1 as expected, while an isoleucine-to-alanine
140 mutation of the SARS-CoV-2 or HKU4 Mac1 did not impact enzyme activity (9, 35). It remains
141 unclear how these residues impact ADP-ribose binding and ultimately how their biochemical
142 functions relate to virus replication and pathogenesis.

143 In this study, we tested how mutations of the isoleucine (I) and phenylalanine (F) residues
144 in loop 2 of the CoV Mac1 (Fig. 1A-B) to alanine (A) impact both Mac1 biochemical functions
145 and the replication of *Embeco*, *Merbeco*, and *Sarbeco* lineages of *β*-CoVs. While F-A mutations
146 resulted in poor enzyme activity and attenuated viruses, I-A mutations surprisingly led to enhanced
147 ADP-ribose binding with little-to-no effect on its enzyme activity. More remarkably, this enhanced
148 binding was detrimental to its biological function, as recombinant MERS-CoV and SARS-CoV-2
149 viruses with the I-A mutation were highly attenuated. We hypothesize that this isoleucine residue
150 acts as a gate to control ADP-ribose binding and maintain proper enzyme activity during infection.
151 These results provide a unique example where enhancing the biochemical activity of a protein has
152 a negative impact on its biological function.

153 **RESULTS**

154 **Mouse hepatitis virus strain JHM (MHV) F1441A, but not I1440A, has decreased replication**
155 **in cell culture and in mice.** To uncover the relative contributions of the residues in the highly
156 conserved GIF motif of Mac1 in CoV replication and pathogenesis, we first compared the
157 replication of the *Embecovirus* MHV I1440A and F1441A mutations to WT and a previously
158 characterized mutant virus, N1347A. Previously, we found that N1347A replicates normally in
159 most cell lines susceptible to MHV but replicates poorly in primary macrophages and in mice (26,
160 32). Here, we tested the replication of recombinant viruses in several different cell types that are
161 susceptible to MHV including: a mouse astrocyte cell line (DBT), a mouse fibroblast cell line
162 (L929), and primary bone-marrow cells differentiated into M2 macrophages. M2 macrophages
163 were used as they have a more pronounced phenotype with the MHV N1347A virus than M0
164 macrophages, making them an ideal cell type to study mutant virus replication. As expected, the
165 F1441A mutation had decreased production of infectious virus in all cell types and in mice, with
166 defects seen at peak titers of 2.7-fold in DBT cells, 4.3-fold in L929 cells, and 21.7-fold in M2
167 macrophages (Fig. 2A-C). We previously found that a knockout (KO) of PARP12 can restore the
168 infectious virus production of N1347A, therefore we also tested the ability of F1441A to replicate
169 in PARP12 KO M2 BMDMs (Fig. 2D). In the absence of PARP12, F1441A infectious virus
170 production increased by 9.3-fold, indicating that PARP12 contributes to the restriction of this virus,
171 much like N1347A. In contrast, I1440A produced virus at WT levels in all cell types and at all
172 time points (Fig. 2A-D).

173 We hypothesized that the importance of the isoleucine residue may become more apparent
174 *in vivo*, so we tested the ability of these MHV mutant viruses to replicate and cause severe
175 encephalitis in mice. C57BL/6 mice were infected intranasally with 10^4 PFU of each virus and

176 were monitored for weight loss and survival over 12 days, and viral loads in the brain were
177 measured at day 5 post-infection. The F1441A mutant was attenuated in mice as only 50% of the
178 mice succumbed to infection, while the other half recovered after losing ~10% of their body weight
179 (Fig. 3A and B). This attenuation of F1441A was also demonstrated in the disease scores, as they
180 began to return to normal by day 8 (Fig. 3C). Furthermore, F1441A virus infected mice had ~7.5
181 fold lower viral loads than WT virus infected mice (Fig. 3D). These titers were highly variable,
182 reflecting the fact that 50% of the mice survived. In contrast, I1440A infected mice all succumbed
183 to disease by 9 dpi, and much like the cell culture results the I1440A viral loads were nearly
184 equivalent to WT virus in mice (Fig. 3A-D). Taken together, this indicates that F1441 is required
185 for efficient virus replication and disease progression, while mutation of the I1440 residue does
186 not impact MHV replication or pathogenesis. The lack of any impact of the I1440A mutation on
187 MHV replication or pathogenesis was surprising, considering the extreme conservation of this
188 residue through all CoVs (6).

189 **MERS-CoV I1238A and F1239A proteins have opposing effects on Mac1 biochemical**
190 **activities.** To determine how these mutations impact the biochemical activities of Mac1, we aimed
191 to purify Mac1 protein with these mutations and utilize *in vitro* assays to measure ADP-
192 ribosylhydrolase and ADP-ribose binding activity of each mutant protein. Multiple attempts to
193 produce MHV Mac1 protein failed, so we engineered these mutations into the *Merbecovirus*
194 MERS-CoV and the *Sarbecovirus* SARS-CoV-2 Mac1 recombinant proteins, as we've previously
195 produced WT Mac1 proteins from each virus (7). We first produced soluble I1238A and F1239A
196 MERS-CoV Mac1 proteins and performed isothermal titration calorimetry (ITC) to measure
197 Mac1-ADP-ribose binding. ITC measures the release or absorption of energy during a binding
198 reaction and has been used extensively to measure macrodomain-ADP-ribose interactions (7, 23,

199 27, 36, 37). Compared to WT protein, the F1239A protein bound to free ADP-ribose with a
200 substantially higher K_D value (60 μM vs. 7.2 μM) indicating reduced binding ability. In contrast,
201 the I1238A protein bound to ADP-ribose with a K_D nearly equivalent to that of WT (12.7 μM vs
202 7.2 μM) (Fig. 4A). In addition to ITC, we also performed an AlphaScreen assay, as previously
203 described (38-40), to determine the ability of each protein to bind to a non-cleavable ADP-
204 ribosylated peptide. This peptide was chosen considering the robust signal that it produces in the
205 presence of Mac1 proteins (38). Similar to the ITC assay, the F1239A Mac1 had reduced
206 AlphaScreen counts at all concentrations of protein tested as compared to WT protein, indicating
207 poor binding to the ADP-ribosylated peptide (Fig. 4B). Remarkably, the I1238A Mac1 protein had
208 substantially increased AlphaScreen counts at all concentrations of protein tested, indicating that
209 this mutation has enhanced binding to an ADP-ribosylated peptide (Fig. 4B). As a control, we
210 found that the I1238A protein did not bind to the unmodified peptide (data not shown). To further
211 test this observation, we performed a competition assay by adding increasing amounts of ADP-
212 ribose to the reaction. ADP-ribose inhibited the peptide-ADP-ribose interaction of WT MERS-
213 CoV protein with an average IC_{50} value, of 0.155 μM, while it had a much higher IC_{50} value of 1.6
214 μM for the I1238A protein. These results demonstrate that I1238A had a stronger interaction with
215 an ADP-ribosylated peptide, but not free ADP-ribose, than WT protein (Fig. 4C).

216 We next tested the ability of the MERS-CoV I1238A and F1238A Mac1 proteins to
217 hydrolyze mono-ADP-ribose (MAR) from protein as previously described (7). The WT, I1238A,
218 and F1239A Mac1 proteins were incubated with MARylated PARP10 at a 1:5 enzyme to substrate
219 ([E]/[S]) ratio, and the reaction was stopped at several timepoints to determine the ability of each
220 protein to hydrolyze MAR. As a control, MARylated PARP10 was collected at the first (0 min)
221 and the final (30 min) timepoints. Over the course of 30 minutes, the MERS-CoV I1238A Mac1

222 protein decreased the level of MARylated PARP10 to levels similar to that of the MERS-CoV WT
223 Mac1 protein, while the MERS-CoV F1239A Mac1 protein did not efficiently remove MAR from
224 PARP10 (Fig. 4D-E). Taken together, we conclude that the MERS-CoV I1238A and F1239A
225 mutations had somewhat opposing effects on the activity of Mac1. While F1239A mutant Mac1
226 protein has decreased ADP-ribose binding and hydrolysis activity, the I1238A Mac1 has at least
227 similar, if not increased ADP-ribose binding, depending on the substrate, with only a modest
228 reduction in enzyme activity compared to the MERS-CoV WT Mac1 (Table 1).

229 **MERS-CoV I1238A and F1239A viruses have decreased virus production in Calu-3 cells.** We
230 next tested the ability of MERS-CoV N1147A, I1238A, and F1239A recombinant viruses to
231 replicate in cell culture. First, using recombination, we inserted a GFP cassette in place of ORF5
232 in the MERS-CoV-MA BAC, as ORF5 quickly mutates in cell culture, which could complicate
233 our results (41, 42). Considering that the I1238A had equivalent or enhanced biochemical activities
234 compared to WT protein, we hypothesized that only the N1147A and F1239A viruses would
235 impact MERS-CoV replication, similar to results seen with MHV (Figs. 2-3). Each mutant virus
236 produced infectious virus near WT levels at 24 and 48 hpi in Vero81 cells, which are unable to
237 produce interferon (IFN) (Fig. 5A). Next, we tested the replication of these viruses in IFN-
238 competent Calu-3 cells, which are human bronchial epithelial cells that are a commonly used cell
239 line for both MERS-CoV and SARS-CoV-2 infections. To our surprise, all 3 viruses replicated
240 poorly in these cells. In Calu3 cells each virus had between 2.1 and 2.5-fold lower levels of
241 infectious virus produced than WT virus at 48 hpi, and had between 8.5 and 10.5-fold lower levels
242 of infectious virus production at 72 hpi (Fig. 5B). As each mutation led to a nearly identical
243 reduction in virus replication, we conclude that each of these residues is critical for MERS-CoV

244 replication in cell culture, and that the defect of the I1238A virus could be due to enhanced ADP-
245 ribose binding (Table 1).

246 **SARS-CoV-2 I1153A and F1154A have increased ADP-ribose binding activity.** The MERS-
247 CoV data indicated that increased ADP-ribose binding activity may lead to replication defects in
248 culture. However, the I1238A MERS-CoV mutant that had increased ADP-ribose binding, had at
249 least a modest defect in enzyme activity, which could account for its poor replication (Table 1).
250 To further test the hypothesis that increased ADP-ribose binding could be detrimental to infection,
251 we engineered these mutations in SARS-CoV-2 to analyze their impact on Mac1 biochemical
252 functions and viral replication. We produced soluble I1153A and the F1154A SARS-CoV-2 Mac1
253 proteins and first performed ITC to determine the ADP-ribose binding ability of each Mac1 mutant
254 protein. Interestingly, both the SARS-CoV-2 I1153A and the F1154A Mac1 proteins had increased
255 binding to free ADP-ribose, with K_D values of 5.49 μM and 5.11 μM, respectively, compared to
256 the K_D value of 16.8 μM for WT protein (Fig. 6A). To confirm these results with free ADP-ribose,
257 we performed a differential scanning fluorimetry assay, which measures the thermal stability of a
258 protein in the presence of a substrate. Again, both the I1153A and F1154A proteins had increased
259 binding as compared to WT protein in this assay (Fig. 6B). Finally, we tested the ability of each
260 protein to bind to the ADP-ribosylated peptide in the AlphaScreen assay. Unfortunately, the
261 F1154A, but not the I1153A protein strongly bound to the control, unmodified peptide (Fig. 6C).
262 Thus, we were unable to evaluate the ability of F1154A protein's ability to bind ADP-ribosylated
263 peptide. However, the I1153A protein had significantly increased binding to the ADP-ribosylated
264 peptide compared to the WT Mac1 protein (Fig. 6D). We conclude that both the I1153A and
265 F1154A proteins have increased binding to ADP-ribose *in vitro*.

266 Next, we tested the ability of each SARS-CoV-2 protein to remove MAR from MARylated
267 PARP10, again at a 1:5 [E]/[S] ratio to account for defects in enzyme turnover. Like MERS-CoV
268 F1239A, SARS-CoV-2 F1154A had only modest hydrolysis activity. In contrast, I1153A Mac1
269 protein had robust enzymatic activity, which was virtually indistinguishable from WT protein (Fig.
270 6E-F), which is consistent with previously published results (9). These results demonstrate that the
271 I1153A and F1154A both have enhanced ADP-ribose binding, but that only F1154A has reduced
272 enzymatic activity (Table 1).

273 As many previous studies on the role of Mac1 in virus replication include the highly
274 conserved asparagine-to-alanine mutation, we also generated an N1062A SARS-CoV-2 Mac1
275 protein. While CoVs with this mutation are easily recovered and often grow like WT virus, unlike
276 full deletion viruses (24, 34), for unknown reasons this recombinant protein is highly unstable.
277 Thus, several modifications to the normal protocol were made to create a small amount of soluble
278 protein. While the small amount of protein did not allow for ITC measurements, this protein had
279 similar ADP-ribose binding properties as WT protein, as determined in combination by the
280 alphascreen, ADP-ribose competition, and differential scanning fluorimetry assays (Fig. 6G-I). In
281 contrast, this protein had substantially reduced ADP-ribosylhydrolase activity (Fig. 6J-K),
282 indicating that this mutation primarily impacts the enzyme activity of Mac1. Previously published
283 data also supports the hypothesis that this mutation primarily impacts the enzyme activity of Mac1
284 (11, 12, 23, 29, 31, 36). Thus, a combination of recombinant N1062A, I1153A, and F1154A
285 SARS-CoV-2 viruses may be useful in defining the role of ADP-ribose binding and hydrolysis
286 during infection, as N1062A has similar binding and reduced enzyme activity, F1154A has
287 increased binding and reduced enzyme activity, and I1153A has only increased binding (Table 1).

288 **I1153A and F1154A mutations increase the sensitivity of SARS-CoV-2 to IFNγ.** We
289 previously reported that a Mac1 deleted SARS-CoV-2 replicates at levels similar to WT virus, but
290 was highly sensitive to IFNγ, but not IFN*β* pretreatment in Calu-3 cells (24). We next tested the
291 ability of I1153A and F1154A recombinant viruses to produce infectious virus in the presence and
292 absence of IFNγ in both A549-ACE2 and Calu-3 cells. Without IFNγ pre-treatment at 48 hpi, both
293 I1153A and F1154A produce infectious virus at WT levels, as expected (Fig. 8A). In contrast,
294 there is a substantial decrease in the production of both I1153A and F1154A infectious virus
295 compared to WT SARS-CoV-2 in the presence of IFNγ in both cell lines (Fig. 8A-B). Furthermore,
296 mutation at the N1062 residue has increased sensitivity to IFNγ as well, though not as severe as
297 the I1153A and F1154A mutant viruses (24). We conclude that the I1153A and F1154A mutations
298 are detrimental for the ability of SARS-CoV-2 to replicate efficiently in the presence of IFNγ.
299 **SARS-CoV-2 I1153A and F1154A are attenuated in K18-ACE2 mice.** Next, we tested whether
300 the I1153A and F1154A Mac1 mutations would be detrimental to SARS-CoV-2 infection in mice.
301 Previously, a SARS-CoV-2 Mac1 deletion virus was shown to be extremely attenuated in K18-
302 ACE2 mice, while the N1062A mutant was mildly attenuated, with approximately 50% of mice
303 surviving the infection (24, 29). We hypothesized that like the SARS-CoV-2 N1062A mutant, there
304 would be at least partial attenuation of I1153A and F1154A viruses in mice. Following an intranasal
305 infection, both the SARS-CoV-2 I1153A and F1154A viruses were extremely attenuated in mice,
306 as they did not cause any weight loss or lethal disease in mice, similar to *Δ*Mac1, whereas WT
307 SARS-CoV-2 causes 100% mortality by 9 dpi (Fig. 9A-B). Viral titers were reduced by ~4-5 fold
308 at 1 dpi (Fig. 9C), and by 8 dpi both the I1153A and F1154A viruses were cleared from the lungs
309 of mice (Fig. 9D). Furthermore, mice infected with these viruses had reduced signs of disease,
310 such as bronchointerstitial pneumonia, edema, or fibrin, as measured by H&E staining (Fig. 9E-

311 F). Finally, both I1153A and F1154A infected mice had significantly increased levels of IFN-I,
312 IFN-III, ISG15, and CXCL-10 mRNA, similar to ∆Mac1 infection levels (Fig. 9G) (29, 34). These
313 results demonstrate that both I1153A and F1154A mutations are detrimental to SARS-CoV-2
314 replication and pathogenesis *in vivo*.

315 In total, while the highly conserved isoleucine and phenylalanine mutations in MERS-CoV
316 and SARS-CoV-2 have different effects on Mac1 biochemical activities *in vitro*, their impact on
317 virus replication and pathogenesis were remarkably similar (Table 1). The simplest explanation is
318 that enhanced ADP-ribose binding has a detrimental effect on Mac1's function, and that the
319 conserved isoleucine residue acts to control ADP-ribose binding to allow for optimal function. But
320 how does this isoleucine residue control ADP-ribose binding? Prior NMR data from the
321 Venezuelan equine encephalitis virus (VEEV) macrodomain indicated that prior to ADP-ribose
322 binding there is a significant transition that increases the distance between loop 1 and loop 2 from
323 7 to 10 Å to accommodate ADP-ribose as a substrate (43). We hypothesized that the I1153A
324 protein has increased binding because the protein no longer requires this transition to bind ADP-
325 ribose due to the loss of the bulky isoleucine side chain. To support this hypothesis, we performed
326 a molecular dynamic (MD) simulation of the I1153A and WT proteins in the presence and absence
327 of ADP-ribose and measured the 1 ns running average distance between the I or A 1153 residue
328 and G1069 (Fig. 10A-C). In the absence of ADP-ribose, the mutant protein (A1153) consistently
329 sampled conformations containing a larger distance between these residues, around or longer than
330 ~7.5 Å, which results in a largely open crevice between the two loops (Fig. 10A). In contrast, the
331 distance between these residues for the WT protein (I1153) was more often less, even sampling
332 distances below 5 Å (Fig. 10A), and the crevice appears mostly in a closed state, only occasionally
333 opening wide enough to allow for ADP-ribose binding (Fig. 10B-C). However, in the presence of

334 ADP-ribose, these residues were nearly the same distance apart in WT and I1153A Mac1 proteins,
335 ~7.5-8 Å, throughout the simulation, indicating that the mutation may not impact the ability of
336 ADP-ribose to exit the binding site. These results suggest that the isoleucine , due to its bulky side-
337 chain, controls the ability of ADP-ribose to enter, but not exit, the ADP-ribose binding domain.

338 **DISCUSSION**

339 Research on the CoV Mac1 domain over the last two decades has established this protein
340 domain as critical for the replication and pathogenesis of CoVs (44). However, the relative
341 contributions of its two major biochemical activities, ADP-ribose binding and deMARylation, to
342 its function during infection has remained unclear. Most research on the CoV Mac1 domain has
343 utilized the mutation of a highly-conserved Asn-to-Ala to understand its role in viral replication
344 and pathogenesis. This mutation nearly eliminates the ADP-ribosylhydrolase activity of SARS-
345 CoV Mac1, however, it was previously not clear how much this mutation impacts ADP-ribose
346 binding. Results from archaeal and alphavirus macrodomains have indicated that mutation of the
347 orthologous asparagine residue in those proteins to alanine modestly reduces ADP-ribose binding
348 (23, 36). Here we created an N1062A Mac1 protein from SARS-CoV-2 and found that it had a
349 severe defect in enzyme activity, but only had a modest, but significant reduction in ADP-ribose
350 binding compared to WT protein (Fig. 7). This confirms that this residue plays a large role in ADP-
351 ribosylhydrolase activity but only moderately impacts ADP-ribose binding. These results further
352 indicate that phenotypes associated with this mutation, including increased IFN production and
353 enhanced sensitivity to IFNβ and IFNγ, are likely due to the loss of ADP-ribosylhydrolase activity,
354 especially considering a SARS-CoV-2 aspartic acid to alanine mutation (D1044A), predicted to
355 dramatically reduce binding, was not sensitive to IFNγ and the orthologous MHV mutation,
356 D1329A does not substantially increase IFNβ production (7, 34).

357 This study focused on the isoleucine and phenylalanine residues located in loop 2 of Mac1,
358 near this asparagine residue, and their roles in the biochemical activites of Mac1 and how they
359 impact CoV replication and pathogenesis. The isoleucine in loop 2 of the CoV Mac1 protein has
360 been described as a bridge that extends from loop 2 to loop 1 that covers the phosphate binding
361 domain of Mac1, forming a narrow channel that might impact binding or hydrolysis (7, 10, 11,
362 35). Furthermore, this residue participates in the transition of these loops from the apo form to the
363 ADP-ribose bound form (43), again indicating that this residue may impact ADP-ribose binding.
364 Somewhat surprisingly, we found that an I-A mutation instead led to enhanced ADP-ribose binding
365 based on a peptide-ADP-ribose binding assay for both the MERS-CoV and SARS-CoV-2 Mac1
366 proteins (Figs. 4B-C, 6A-B). Modeling data indicates that with this mutation, the distance between
367 the two loops is consistently large enough that Mac1 can likely accept substrates more readily, as
368 opposed to Mac1 with the isoleucine (Fig. 10A-C). Following ADP-ribose binding, the I-A
369 mutation does not appear to impact the distance between the loops, perhaps explaining why the
370 hydrolysis activity of Mac1 was not affected for either Mac1 protein. These results suggest that
371 the isoleucine residue serves as a gate to control ADP-ribose binding levels.

372 In contrast, the phenylalanine residue forms van der Waals interactions with the distal
373 ribose, and similar to the nearby asparagine residue, appears to help position the ribose for
374 hydrolysis. Biochemical data has supported those predictions, as mutations of this residue
375 generally result in substantial loss of hydrolysis activity, which we observed here for both the
376 MERS-CoV and SARS-CoV-2 Mac1 proteins (Figs. 4D-E, 6C-D). Interestingly, the F-A mutation
377 had diverse roles in ADP-ribose binding. For MERS-CoV Mac1, this mutation led to reduced
378 binding, while for SARS-CoV-2 this mutation enhanced both free and peptide-conjugated ADP-
379 ribose binding. As the phenylalanine residue resides just outside the terminal ribose, it's

380 conceivable that in some cases this residue may occlude ADP-ribose binding during its transitions,
381 while in others it may be just far enough away to not impact the ability of ADP-ribose to enter the
382 binding pocket (7, 43) Furthermore, an orthologous tyrosine to alanine mutation in the CHIKV
383 macrodomain, Y114A, also led to enhanced ADP-ribose binding, indicating that this residue helps
384 control ADP-ribose binding in multiple macrodomains. While it's unclear how these identical
385 mutations in the MERS-CoV and SARS-CoV-2 Mac1 proteins had opposing effects on ADP-
386 ribose binding, it highlights the difficulty in attributing specific biochemical roles for individual
387 residues from one macrodomain to another. In addition, there are several limitations to our
388 approaches. As there are no known substrates of Mac1 in infection, we use artificial substrates for
389 our *in vitro* assays. These include free ADP-ribose, the product of Mac1's hydrolytic function, an
390 ADP-ribosylated peptide using a random peptide sequence, and an auto-MARylated PARP10
391 protein. However, these are standard assays in the field (9, 23, 27, 35, 45, 46). Furthermore, our
392 modeling data is based on molecular dynamic simulations approximated using the crystal structure
393 of the SARS-CoV-2 Mac1 protein, as no crystal structure exists for the I1153A mutation, and no
394 NMR data is available for either protein. Finally, free ADP-ribose produced during the de-ADP-
395 ribosylation assays could impact the assay, though our deADP-ribosylation experiments performed
396 at a low [E]/[S] ratio suggests that this is not the case (Figs. 4, 6).

397 Both MERS-CoV and SARS-CoV-2 I-A and F-A mutations were equally attenuated in both
398 cell culture and in mice despite having somewhat distinct biochemical properties (Figs. 5, 7, 8).
399 The MERS-CoV mutant viruses replicated normally in Vero81 cells but replicated poorly in Calu-
400 3 cells at levels similar to the N1147A virus. Furthermore, both F-A and I-A SARS-CoV-2 mutant
401 viruses replicated poorly following IFN-γ treatment and induced high levels of IFN and ISG levels
402 following infection in mice, again demonstrating that despite having unique biochemical

403 properties, these mutations led to very similar virological phenotypes (Figs. 7, 9). There are several
404 potential hypotheses that might explain this, and we will outline some of the possibilities here. Our
405 first hypothesis is that increasing ADP-ribose binding could lead to decreased enzyme activity
406 during infection. Why might an increase in ADP-ribose binding lead to reduced enzyme activity
407 during infection? One possibility is that enhanced binding would negatively affect enzyme
408 turnover. However, our *in vitro* enzyme assays were performed at an [E]/[S] ratio of 1:5, indicating
409 that the mutant protein has largely normal enzyme turnover. ADP-ribose can be covalently attached
410 to several different amino acids, including cysteine, serine, arginine, glutamic and aspartic acid,
411 but the MacroD2 class of macrodomains primarily removes ADP-ribose from acidic residues.
412 Therefore, a second hypothesis is that enhancing the ADP-ribose binding abilities of Mac1 may
413 cause it to bind to proteins with ADP-ribose attached at non-acidic residues that it can't remove
414 and are not relevant for virus infection. For instance, during infection WT Mac1 primarily engages
415 with either anti- or pro-viral proteins that are MARylated on an acidic residue. Mac1 removes these
416 modifications, which promotes virus replication and pathogenesis. In contrast, Mac1 I-A may bind
417 non-specifically to proteins MARylated at non-acidic residues, such as serine or asparagine,
418 reducing its ability to engage with its primary targets. In this case, Mac1 becomes stuck to
419 irrelevant targets, while its main target proteins remain ADP-ribosylated, leading to reduced virus
420 replication (Fig. 10D). However, this is not the only possible hypothesis. Additional hypotheses
421 include but are not limited to: *i)* Enhanced ADP-ribose binding enables Mac1 to bind with
422 additional ADP-ribosylated protein or RNA substrates, which is detrimental to infection; *ii)* the I-
423 A mutation could enhance the binding to non-ADP-ribosylated proteins, such as PLPro, which was
424 previously shown to bind the MHV Mac1 protein (47); and *iii)* the I-A mutation could either
425 increase, or decrease the enzyme activity of Mac1 for alternative substrates, such as NAD^+, ADP-

426 ribose-1'-phosphatase, or O-acetyl-ADP-ribose (11, 31, 48). CoV infection can dysregulate the
427 NAD^+ system and reduce NAD^+ levels. We found that NAD^+ levels are reduced following MHV
428 infection and that this depletion enhances MHV Mac1 mutant virus replication, while others have
429 shown that NAD^+ enhancing treatments provide mice some level of increased protection from
430 SARS-CoV-2 (49-51). However, macrodomains are not known to be major consumers of NAD^+,
431 thus this possibility seems unlikely. Furthermore, there's no indication that ADP-ribose-1'-
432 phosphatase, or O-acetyl-ADP-ribose impact CoV infection. Additional experiments will need to
433 be designed to demonstrate how the I-A mutation results in attenuated virus replication.

434 The function of the isoleucine residue of the MHV Mac1 protein appears to be unique, as
435 the mutation of I-A had little-to-no impact on virus replication. As we have been unable to purify
436 the WT MHV Mac1 protein in bacteria, we can only speculate as to how this mutation impacts
437 ADP-ribose binding and hydrolysis. The simplest hypothesis is that this mutation does not enhance
438 ADP-ribose binding as it did for MERS-CoV or SARS-CoV-2. Alternatively, as MHV appears to
439 be highly dependent on the ADP-ribose binding function of Mac1 (24, 34), an increase in ADP-
440 ribose binding may have some beneficial outcome that counteracts the negative effects of this
441 mutation, resulting in a virus that replicates much like WT. Conversely, the F1441A mutant virus
442 replicates poorly in all cells tested and was attenuated in mice, similar to a D1329A mutant virus,
443 a mutation predicted to largely impact ADP-ribose binding. In addition, it was partially, but not
444 fully, rescued in PARP12 KO cells, which we previously found rescued N1347A, but had no effect
445 on D1329A. Thus, based on these and prior results with N1347A and D1329A, we hypothesize
446 that this mutation reduces both enzyme and binding activity, similar to the MERS-CoV F1239A
447 Mac1 protein.

448 These results provide new insights into how Mac1 regulates ADP-ribose binding for its
449 benefit, which could have important implications for the development of inhibitors targeting Mac1.
450 Finally, these mutations could be used to help identify the specific targets of Mac1 during an
451 infection, which will lead to a better understanding of the mechanisms used by mammalian cells
452 to counter virus infection.

453 **METHODS**

454 **Plasmids.** MERS-CoV Mac1 (residues 1110-1273 of pp1a) and mutations were cloned into
455 pET21a+ with a C-terminal His tag. SARS-CoV-2 Mac1 (residues 1023-1197 of pp1a) was cloned
456 into the pET30a+ expression vector with an N-terminal His tag and a TEV cleavage site (Synbio).
457 PARP10-CD was cloned into a pGEX4T expression vector with an N-terminal GST tag and was
458 previously described (kindly provided by Dr. Ivan Ahel, University of Oxford) (52).

459 **Protein Expression and Purification.** A single colony of *E. coli* cells BL21 C41 (DE3) or pRARE
460 (DE3) containing plasmids harboring the constructs of the macrodomain proteins was inoculated
461 into 10 mL LB media and grown overnight at 37°C with shaking at 250 rpm. For most proteins,
462 the overnight culture was transferred to a shaker flask containing TB media at 37°C until the
463 OD600 reached 0.7. The proteins were either induced with either 0.4 mM (SARS-CoV-2 proteins)
464 or 0.05 mM (MERS-CoV proteins) IPTG at 17°C for 20 hours. Cells were pelleted at 3500 × g for
465 10 min and frozen at -80°C. Frozen cells were thawed at room temperature, resuspended in 50 mM
466 Tris (pH 7.6), 150 mM NaCl, and sonicated using the following cycle parameters: Amplitude:
467 50%, Pulse length: 30 seconds, Number of pulses: 12, while incubating on ice for >1min between
468 pulses. The soluble fraction was obtained by centrifuging the cell lysate at 45,450 × g for 30
469 minutes at 4°C. The expressed soluble proteins were purified by affinity chromatography using a
470 5 ml prepacked HisTrap HP column on an AKTA Pure protein purification system (GE
471 Healthcare). The fractions were further purified by size-exclusion chromatography (SEC) with a
472 Superdex 75 10/300 GL column equilibrated with 20mM Tris (pH 8.0), 150 mM NaCl and the
473 protein sized as a monomer relative to the column calibration standards. For the SARS-CoV-2
474 N1062A protein several modifications to this protocol were made to obtain stable soluble protein.
475 First, the overnight culture was transferred to LB instead of TB and grown to OD600 0.5 before

476 the protein was induced with 0.05 mM IPTG at 17°C for 20 hours. Cells were resuspended in water
477 prior to sonication. Tris and NaCl were added after sonication. The cell lysate was then incubated
478 with HIS-select HF Nickel Affinity Gel (Millipore-Sigma) overnight, rotating at 4°C. The lysate
479 was then passed into gravity flow chromatography. Columns were washed with 0.5M NaCl and
480 50 mM Tris-Cl pH 8 and eluted with 0.5 ml of elution buffer with 0.1 M of Imidazole. Following
481 elution, the protein was immediately purified by size-exclusion chromatography as described
482 above. The expression of PARP10 CD protein was previously described (7).

483 **Isothermal Titration Calorimetry.** All ITC titrations were performed on a MicroCal PEAQ-ITC
484 instrument (Malvern Pananalytical Inc., MA). All reactions were performed in 20 mM Tris pH 7.5,
485 150 mM NaCl using 100 μM of all macrodomain proteins at 25°C. Titration of 2 mM ADP-ribose
486 or ATP (MilliporeSigma) contained in the stirring syringe included a single 0.4 μL injection,
487 followed by 18 consecutive injections of 2 μL. Data analysis of thermograms was analyzed using
488 one set of binding sites model of the MicroCal ITC software to obtain all fitting model parameters
489 for the experiments. MERS-CoV and SARS-CoV-2 WT protein ITC data was previously published
490 (7). These experiments were performed alongside the mutant proteins, thus serving as appropriate
491 controls.

492 **Differential Scanning Fluorimetry (DSF)**. Thermal shift assay with DSF involved use of
493 LightCycler® 480 Instrument (Roche Diagnostics). In total, a 15 μL mixture containing 8X
494 SYPRO Orange (Invitrogen), and 10 μM macrodomain protein in buffer containing 20 mM Hepes,
495 NaOH, pH 7.5 and various concentrations of ADP-ribose were mixed on ice in 384-well PCR plate
496 (Roche). Fluorescent signals were measured from 25 to 95 °C in 0.2 °C/30-s steps (excitation, 470-
497 505 nm; detection, 540-700 nm). Data evaluation and Tm determination involved use of the Roche

498 LightCycler® 480 Protein Melting Analysis software, and data fitting calculations involved the
499 use of single site binding curve analysis on Graphpad Prism.
500 **AlphaScreen (AS) Assay.** The AlphaScreen reactions were carried out in 384-well plates
501 (Alphaplate, PerkinElmer, Waltham, MA) in a total volume of 40 µL in buffer containing 25 mM
502 HEPES (pH 7.4), 100 mM NaCl, 0.5 mM TCEP, 0.1% BSA, and 0.05% CHAPS. All reagents
503 were prepared as 4X stocks and 10 µL volume of each reagent was added to a final volume of 40
504 µL. All compounds were transferred acoustically using ECHO 555 (Beckman Inc) and
505 preincubated after mixing with purified His-tagged macrodomain protein (250 nM) for 30 min at
506 RT, followed by addition of a 10 amino acid biotinylated and ADP-ribosylated peptide
507 [ARTK(Bio)QTARK(Aoa-RADP)S] (Cambridge peptides) (625 nM). After 1h incubation at RT,
508 streptavidin-coated donor beads (7.5 µg/mL) and nickel chelate acceptor beads (7.5 µg/mL);
509 (PerkinElmer AlphaScreen Histidine Detection Kit) were added under low light conditions, and
510 plates were shaken at 400 rpm for 60 min at RT protected from light. Plates were kept covered and
511 protected from light at all steps and read on BioTek plate reader using an AlphaScreen 680
512 excitation/570 emission filter set. For data analysis, the percent inhibition was normalized to
513 positive (DMSO + labeled peptide) and negative (DMSO + macrodomain + peptide, no ADPr)
514 controls. The IC_{50} values were calculated via four-parametric non-linear regression analysis
515 constraining bottom (=0), top (=100), & Hillslope (=1) for all curves.
516 **MAR Hydrolase Assays**. First, a 10 µM solution of purified PAPR10-CD protein was incubated
517 for 20 minutes at 37°C with 1 mM final concentration of β-Nicotinamide Adenine Dinucleotide (β
518 NAD^{+}) (Millipore-Sigma) in a reaction buffer (50 mM HEPES, 150 mM NaCl, 0.2 mM DTT, and
519 0.02% NP-40). MARylated PARP10 was aliquoted and stored at -80°C. Next, a 0.5 (I-A/F-A) or 5
520 (N/A) µM solution of MARylated PARP10-CD and 0.1 (I-A/F-A) or 1 (N-A) µM purified Mac1

521 protein was added in the reaction buffer (50 mM HEPES, 150 mM NaCl, 0.2 mM DTT, and 0.02%
522 NP-40) and incubated at 37 ºC for indicated times. The reaction was stopped with addition of 2X
523 Laemmli sample buffer containing 10% β-mercaptoethanol. Protein samples were heated at 95ºC
524 for 5 minutes before loading and separated onto SDS-PAGE cassette (Thermo Fisher Scientific
525 Bolt™ 4-12% Bis-Tris Plus Gels) in MES running buffer. For direct protein detection, the SDS-
526 PAGE gel was stained using InstantBlue® Protein Stain (Expedeon). For immunoblotting, the
527 separated proteins were transferred onto polyvinylidene difluoride (PVDF) membrane using
528 iBlot™ 2 Dry Blotting System (ThermoFisher Scientific). The blot was blocked with 5% skim
529 milk in PBS containing 0.05% Tween-20 and probed with anti-mono ADP-ribose binding reagent
530 MABE1076 (α-MAR) (Millipore-Sigma) and anti-GST tag monoclonal antibody MA4-004
531 (ThermoFisher Scientific). The primary antibodies were detected with secondary infrared anti-
532 rabbit and anti-mouse antibodies (LI-COR Biosciences). All immunoblots were visualized using
533 Odyssey® CLx Imaging System (LI-COR Biosciences). The images were quantitated using Image
534 J (National Institutes for Health (NIH)) or Image Studio software.
535 **Molecular Dynamics (MD) Simulations.** 25 ns simulations were performed for WT and I1153A
536 protein in the presence and absence of ADP-ribose using GROMACS 2019.4 (53). Protein
537 structures used were ADP-ribose-bound SARS-2-CoV Mac1, PDB 6W02 (46), and unbound
538 SARS-2-CoV Mac1, PDB 7KQO (54). The simulations were prepared, including virtual
539 mutagenesis, using CHARMM-GUI's Solution Builder (55), which was used to build a solvated,
540 rectangular box around one protein, parameterize the ligand, add ions to neutralize the system, set
541 up periodic boundary conditions, and generate the files to perform a gradient based minimization,
542 100 ps equilibration with a NVT ensemble, and then a 25 ns production run with an NPT ensemble
543 at 303.15 K.

544 **Cell Culture and Reagents.** Vero E6, Huh-7, Vero81, DBT, L929, HeLa cells expressing the
545 MHV receptor carcinoembryonic antigen-related cell adhesion molecule 1 (CEACAM1) (HeLa-
546 MHVR), Baby Hamster Kidney cells expressing the mouse virus receptor CEACAM1 (BHK-
547 MVR) (all gifts from Stanley Perlman, University of Iowa) and A549-ACE2 cells (a gift from
548 Susan Weiss, University of Pennsylvania), were grown in Dulbecco's modified Eagle medium
549 (DMEM) supplemented with 10% fetal bovine serum (FBS). Calu-3 cells (ATCC) were grown in
550 MEM supplemented with 20% FBS. Bone marrow-derived macrophages (BMDMs) sourced from
551 PARP12$^{+/+}$ and PARP12$^{-/-}$ mice were differentiated into M0 macrophages by incubating cells in
552 Roswell Park Memorial Institute (RPMI) media supplemented with 10% FBS, sodium pyruvate,
553 100 U/ml penicillin and 100 mg/ml streptomycin, L-glutamine, M-CSF (Genscript) for six days.
554 Then to differentiate into M2 macrophages, IL-4 (Peprotech Inc.) was added for 1 day. Cells were
555 washed and replaced with fresh media every other day after the 4th day. Human IFN-γ was
556 purchased from R&D Systems. Cells were transfected with either Polyjet (Amgen) or
557 Lipofectamine 3,000 (Fisher Scientific) per the instructions of the manufacturers.
558 **Generation of Recombinant pBAC-JHMV, pBAC-MERS-CoV, and pBAC-SARS-CoV-2**
559 **Constructs.** All recombinant pBAC constructs were created using Red recombination with several
560 previously described CoV BACs as previously described (41). These include the WT-SARS-CoV-
561 2 BAC based off the Wuhan-Hu-1 isolate provided by Sonia Zuñiga, Li Wang, Isabel Sola and
562 Luis Enjuanes (CNB-CSIC, Madrid, Spain) (56), a MERS-CoV mouse-adapted BAC (a gift from
563 Dr. Stanley Perlman) with GFP inserted into ORF5 (57, 58), and an MHV BAC based off of the
564 JHMV isolate (26). Primers used to create each mutation are listed in Table 2.
565 **Reconstitution of Recombinant pBAC-JHMV, pBAC-MERS-CoV, and pBAC-SARS-CoV-**
566 **2-Derived Virus.** All work with SARS-CoV-2 and MERS-CoV was conducted in either the

567 University of Kansas or the Oklahoma State University EHS-approved BSL-3 facilities. To
568 generate SARS- CoV-2 or MERS-CoV, approximately 5×10^5 Huh-7 cells were transfected with
569 2 μg of purified BAC DNA using Lipofectamine 3,000 (Fisher Scientific) as a transfection reagent.
570 SARS-CoV-2 generated from these transfections (p0) was then passaged in Vero E6 (SARS-CoV-
571 2) or Vero 81 (MERS-CoV) cells to generate viral stocks (p1). All p1 stocks were again sequenced
572 by Sanger sequencing to confirm that they retained the correct mutations. To generate MHV-JHM,
573 approximately 5×10^5 BHK-MVR cells were transfected with 1 μg of purified BAC DNA and 1
574 μg of N-protein expressing plasmid using PolyJetTM Transfection Reagent (SignaGen). All I-A
575 and F-A recombinant virus stocks had their full genomes sequenced by either Illumina RNA
576 sequencing using polyA enrichment (MHV and MERS-CoV) or by creating amplicons and
577 performing standard whole genome sequencing (SARS-CoV-2) (SeqCenter). No additional
578 variants were detected in these genomes. Sequencing results will be deposited along with all other
579 data in FigShare.
580 **Mice.** Pathogen-free C57BL/6NJ (B6) and K18-ACE2 C57BL/6 mice were originally purchased
581 from Jackson Laboratories and mice were bred and maintained in the animal care facilities at the
582 University of Kansas and Oklahoma State University. Animal studies were approved by the
583 Oklahoma State University and University of Kansas Institutional Animal Care and Use
584 Committees (IACUC) following guidelines set forth in the Guide for the Care and Use of
585 Laboratory Animals.
586 **Virus Infection.** Cells were infected at the indicated MOIs. All infections included a 1 hr
587 adsorption phase. Infected cells and supernatants were collected at indicated time points and titers
588 were determined. For IFN pretreatment experiments, human IFN-γ was added to Calu-3 or A549-
589 ACE2 cells 18 to 20 h prior to infection and was maintained in the culture media throughout the

590 infection. For MHV mouse infections, 5-8 week-old male and female mice were anesthetized with
591 isoflurane and inoculated intranasally with 1×10^4 PFU recombinant MHV in a total volume of 12
592 µl DMEM. MHV infected mice were scored for disease based on the following scale: 0: normal,
593 0-5% weight loss with normal movement and normal behavior; 1: mild disease, 6-12% weight
594 loss, slightly slower movement, and mild neurological issues including circling, sporadic and
595 sudden jumping/hyperreactivity; 2: moderate disease, 13-20% weight loss, slow movement with
596 notable difficulty, moderate neurological issues including occasional circling or head pressing; 3:
597 severe, >20% decrease in weight, severely reduced mobility, and severe neurological symptoms.
598 Mice were euthanized if any of the conditions for a score of 3 were met. For SARS-CoV-2 mouse
599 infections, 12 to 16-wk-old K18-ACE2 C57BL/6 female mice were lightly anesthetized using
600 isoflurane and were intranasally infected with 2.5×10^4 PFU in 50 µL DMEM. To obtain tissue
601 for virus titers, mice were euthanized on different days post challenge, lungs or brains were
602 removed and homogenized in phosphate buffered saline (PBS), and titers were determined by
603 plaque assay on either Hela-MVR (MHV) or Vero E6 (SARS-CoV-2) cells.
604 **Histopathology.** The lung lobes were perfused and placed in 10% formalin. The lung lobes were
605 then processed for H&E staining. The lung lesions were blindly scored by an American College
606 of Veterinary Pathology Board-certified pathologist. The lesions were scored on a scale of 0 to
607 10% (score 1), 10 to 40% (score 2), 40 to 70% (score 3), and >70% (score 4), and cumulative
608 scores were obtained for each mouse. The lesions scored were bronchointerstitial pneumonia,
609 perivascular inflammation, edema/fibrin, and necrosis.
610 **Real-time qPCR analysis.** RNA was isolated from cells and lungs using TRIzol (Invitrogen) and
611 cDNA was prepared using MMLV-reverse transcriptase as per manufacturer's instructions
612 (Thermo Fisher Scientific). Quantitative real-time PCR (qRT-PCR) was performed on a

613 QuantStudio3 real-time PCR system using PowerUp SYBR Green Master Mix (Thermo Fisher
614 Scientific). Primers used for qPCR were previously described (24). Cycle threshold (C_T) values
615 were normalized to the housekeeping gene hypoxanthine phosphoribosyltransferase (HPRT) by
616 the following equation: $C_T = C_{T(\text{gene of interest})} - C_{T(\text{HPRT})}$. Results are shown as a ratio to HPRT
617 calculated as $2^{-\Delta CT}$.

618 **Statistics.** A Student's *t* test was used to analyze differences in mean values between 2 groups,
619 for multiple group comparisons, a one-way ANOVA was used. All results are expressed as
620 means ± standard errors of the means (SEM) unless stated as standard differentiation (SD). P
621 values of ≤0.05 were considered statistically significant (*, P≤0.05; **, P≤0.01; ***, P≤0.001;
622 ****, P ≤0.0001; ns, not significant).

ACKNOWLEDGEMENTS
We thank Ivan Ahel for providing protein expression plasmids, Stanley Perlman and Susan Weiss for cell lines, Stanley Perlman for critical reading of the manuscript and the MERS-CoV mouse adapted BAC, and Luis Enjuanes and Sonia Zuñiga for the SARS-CoV-2 BAC. We thank Brian Sanderson, the KU Center for Genomics, and the K-INBRE Genomic Data Science Core supposted by the IDeA Program of the NIGMS award number P20GM103418 for help with RNAseq analysis. We thank our funding from the NIH, an NIH Graduate Training grant, the University of Kansas College of Liberal Arts and Sciences, and the University of Kansas Madison and Lila Self graduate programs.

Funding:
National Institutes of Health (NIH) grant R35GM138029 (ARF)
National Institutes of Health (NIH) grant P20GM113117 (ARF)
National Institutes of Health (NIH) grant K22AI134993 (ARF)
National Institutes of Health (NIH) grant P20GM103648 (RC)
NIH Graduate Training at the Biology-Chemistry Interface grant T32GM132061 (CMK)
University of Kansas College of Liberal Arts and Sciences Graduate Research Fellowship (CMK)
University of Kansas Madison and Lila Self Scholarship and Fellowship (JJP)

The funders had no role in study design, data collection and analysis, decision to publish, or preparation of the manuscript.

Author contributions:
Conceptualization: CMK, JJP, YMA, ARF
Data curation: CMK, YMA, AR, JJOC, RG, SM, RC, ARF
Formal analysis: CMK, YMA, AR, JJOC, RG, SM, RC, ARF
Funding acquisition: CMK, RC, ARF
Methodology: CMK, JJP, YMA, AR, JJOC, RG, RK, PG, DKJ, SM, RC, ARF
Investigation: CMK, JJP, YMA, AR, JJOC, RG, RS, PS, SP, PM, RK, DKJ, SM, RC, ARF
Project administration: RC, ARF
Resources: AR, PG, RC, ARF
Visualization: CMK, JJP, YMA, AR, JJOC, RG, RS, PM, RK, DKJ, SM, RC, ARF
Validation: CMK, AR, SM, RC, ARF
Supervision: PG, RC, ARF
Writing—original draft: CMK, ARF
Writing—review & editing: CMK, JJP, YMA, AR, JJOC, RG, RS, PS, SP, PM, RK, DKJ, SM, RC, ARF

The authors have no competing interests.

663 **REFERENCES**

664 1. Perlman S. 2020. Another Decade, Another Coronavirus. N Engl J Med 382:760-762.
665 2. Wang Y, Grunewald M, Perlman S. 2020. Coronaviruses: An Updated Overview of Their
666 Replication and Pathogenesis. Methods Mol Biol 2203:1-29.
667 3. Lei J, Kusov Y, Hilgenfeld R. 2018. Nsp3 of coronaviruses: Structures and functions of a
668 large multi-domain protein. Antiviral Res 149:58-74.
669 4. Wolff G, Limpens R, Zevenhoven-Dobbe JC, Laugks U, Zheng S, de Jong AWM, Koning
670 RI, Agard DA, Grunewald K, Koster AJ, Snijder EJ, Barcena M. 2020. A molecular pore
671 spans the double membrane of the coronavirus replication organelle. Science 369:1395-
672 1398.
673 5. Zimmermann L, Zhao X, Makroczyova J, Wachsmuth-Melm M, Prasad V, Hensel Z,
674 Bartenschlager R, Chlanda P. 2023. SARS-CoV-2 nsp3 and nsp4 are minimal constituents
675 of a pore spanning replication organelle. Nat Commun 14:7894.
676 6. Leung AKL, McPherson RL, Griffin DE. 2018. Macrodomain ADP-ribosylhydrolase and
677 the pathogenesis of infectious diseases. PLoS Pathog 14:e1006864.
678 7. Alhammad YMO, Kashipathy MM, Roy A, Gagne JP, McDonald P, Gao P, Nonfoux L,
679 Battaile KP, Johnson DK, Holmstrom ED, Poirier GG, Lovell S, Fehr AR. 2021. The
680 SARS-CoV-2 Conserved Macrodomain Is a Mono-ADP-Ribosylhydrolase. J Virol 95.
681 8. Rack JG, Perina D, Ahel I. 2016. Macrodomains: Structure, Function, Evolution, and
682 Catalytic Activities. Annu Rev Biochem 85:431-54.
683 9. Rack JGM, Zorzini V, Zhu Z, Schuller M, Ahel D, Ahel I. 2020. Viral macrodomains: a
684 structural and evolutionary assessment of the pharmacological potential. Open Biol
685 10:200237.
686 10. Saikatendu KS, Joseph JS, Subramanian V, Clayton T, Griffith M, Moy K, Velasquez J,
687 Neuman BW, Buchmeier MJ, Stevens RC, Kuhn P. 2005. Structural basis of severe acute
688 respiratory syndrome coronavirus ADP-ribose-1"-phosphate dephosphorylation by a
689 conserved domain of nsP3. Structure 13:1665-75.
690 11. Egloff MP, Malet H, Putics A, Heinonen M, Dutartre H, Frangeul A, Gruez A, Campanacci
691 V, Cambillau C, Ziebuhr J, Ahola T, Canard B. 2006. Structural and functional basis for
692 ADP-ribose and poly(ADP-ribose) binding by viral macro domains. J Virol 80:8493-502.
693 12. Fehr AR, Channappanavar R, Jankevicius G, Fett C, Zhao J, Athmer J, Meyerholz DK,
694 Ahel I, Perlman S. 2016. The Conserved Coronavirus Macrodomain Promotes Virulence
695 and Suppresses the Innate Immune Response during Severe Acute Respiratory Syndrome
696 Coronavirus Infection. mBio 7.
697 13. Li C, Debing Y, Jankevicius G, Neyts J, Ahel I, Coutard B, Canard B. 2016. Viral Macro
698 Domains Reverse Protein ADP-Ribosylation. J Virol 90:8478-86.
699 14. Kar P, Chatrin C, Dukic N, Suyari O, Schuller M, Zhu K, Prokhorova E, Bigot N, Ahel J,
700 Elsborg JD, Nielsen ML, Clausen T, Huet S, Niepel M, Sanyal S, Ahel D, Smith R, Ahel I.
701 2024. PARP14 and PARP9/DTX3L regulate interferon-induced ADP-ribosylation. EMBO
702 J doi:10.1038/s44318-024-00126-0.
703 15. Ribeiro VC, Russo LC, Hoch NC. 2024. PARP14 is regulated by the PARP9/DTX3L
704 complex and promotes interferon gamma-induced ADP-ribosylation. EMBO J
705 doi:10.1038/s44318-024-00125-1.
706 16. Russo LC, Tomasin R, Matos IA, Manucci AC, Sowa ST, Dale K, Caldecott KW, Lehtio
707 L, Schechtman D, Meotti FC, Bruni-Cardoso A, Hoch NC. 2021. The SARS-CoV-2 Nsp3

macrodomain reverses PARP9/DTX3L-dependent ADP-ribosylation induced by interferon signaling. J Biol Chem 297:101041.

17. Dukic N, Stromland O, Elsborg JD, Munnur D, Zhu K, Schuller M, Chatrin C, Kar P, Duma L, Suyari O, Rack JGM, Baretic D, Crudgington DRK, Groslambert J, Fowler G, Wijngaarden S, Prokhorova E, Rehwinkel J, Schuler H, Filippov DV, Sanyal S, Ahel D, Nielsen ML, Smith R, Ahel I. 2023. PARP14 is a PARP with both ADP-ribosyl transferase and hydrolase activities. Sci Adv 9:eadi2687.

18. Suskiewicz MJ, Prokhorova E, Rack JGM, Ahel I. 2023. ADP-ribosylation from molecular mechanisms to therapeutic implications. Cell 186:4475-4495.

19. Luscher B, Ahel I, Altmeyer M, Ashworth A, Bai P, Chang P, Cohen M, Corda D, Dantzer F, Daugherty MD, Dawson TM, Dawson VL, Deindl S, Fehr AR, Feijs KLH, Filippov DV, Gagne JP, Grimaldi G, Guettler S, Hoch NC, Hottiger MO, Korn P, Kraus WL, Ladurner A, Lehtio L, Leung AKL, Lord CJ, Mangerich A, Matic I, Matthews J, Moldovan GL, Moss J, Natoli G, Nielsen ML, Niepel M, Nolte F, Pascal J, Paschal BM, Pawlowski K, Poirier GG, Smith S, Timinszky G, Wang ZQ, Yelamos J, Yu X, Zaja R, Ziegler M. 2021. ADP-ribosyltransferases, an update on function and nomenclature. FEBS J doi:10.1111/febs.16142.

20. Fehr AR, Jankevicius G, Ahel I, Perlman S. 2018. Viral Macrodomains: Unique Mediators of Viral Replication and Pathogenesis. Trends Microbiol 26:598-610.

21. Fehr AR, Singh SA, Kerr CM, Mukai S, Higashi H, Aikawa M. 2020. The impact of PARPs and ADP-ribosylation on inflammation and host-pathogen interactions. Genes Dev 34:341-359.

22. Abraham R, Hauer D, McPherson RL, Utt A, Kirby IT, Cohen MS, Merits A, Leung AKL, Griffin DE. 2018. ADP-ribosyl-binding and hydrolase activities of the alphavirus nsP3 macrodomain are critical for initiation of virus replication. Proc Natl Acad Sci U S A 115:E10457-E10466.

23. Abraham R, McPherson RL, Dasovich M, Badiee M, Leung AKL, Griffin DE. 2020. Both ADP-Ribosyl-Binding and Hydrolase Activities of the Alphavirus nsP3 Macrodomain Affect Neurovirulence in Mice. mBio 11.

24. Alhammad YM, Parthasarathy S, Ghimire R, Kerr CM, O'Connor JJ, Pfannenstiel JJ, Chanda D, Miller CA, Baumlin N, Salathe M, Unckless RL, Zuniga S, Enjuanes L, More S, Channappanavar R, Fehr AR. 2023. SARS-CoV-2 Mac1 is required for IFN antagonism and efficient virus replication in cell culture and in mice. Proc Natl Acad Sci U S A 120:e2302083120.

25. Eriksson KK, Cervantes-Barragan L, Ludewig B, Thiel V. 2008. Mouse hepatitis virus liver pathology is dependent on ADP-ribose-1"-phosphatase, a viral function conserved in the alpha-like supergroup. J Virol 82:12325-34.

26. Fehr AR, Athmer J, Channappanavar R, Phillips JM, Meyerholz DK, Perlman S. 2015. The nsp3 macrodomain promotes virulence in mice with coronavirus-induced encephalitis. J Virol 89:1523-36.

27. McPherson RL, Abraham R, Sreekumar E, Ong SE, Cheng SJ, Baxter VK, Kistemaker HA, Filippov DV, Griffin DE, Leung AK. 2017. ADP-ribosylhydrolase activity of Chikungunya virus macrodomain is critical for virus replication and virulence. Proc Natl Acad Sci U S A 114:1666-1671.

752 28. Parvez MK. 2015. The hepatitis E virus ORF1 'X-domain' residues form a putative
753 macrodomain protein/Appr-1"-pase catalytic-site, critical for viral RNA replication. Gene
754 566:47-53.
755 29. Taha TY, Suryawanshi RK, Chen IP, Correy GJ, McCavitt-Malvido M, O'Leary PC,
756 Jogalekar MP, Diolaiti ME, Kimmerly GR, Tsou CL, Gascon R, Montano M, Martinez-
757 Sobrido L, Krogan NJ, Ashworth A, Fraser JS, Ott M. 2023. A single inactivating amino
758 acid change in the SARS-CoV-2 NSP3 Mac1 domain attenuates viral replication in vivo.
759 PLoS Pathog 19:e1011614.
760 30. Aguilar EG, Paniccia G, Adura C, Singer ZS, Ashbrook AW, Razooky BS, Rice CM,
761 MacDonald MR. 2022. Sindbis Macrodomain Poly-ADP-Ribose Hydrolase Activity Is
762 Important for Viral RNA Synthesis. J Virol 96:e0151621.
763 31. Putics A, Filipowicz W, Hall J, Gorbalenya AE, Ziebuhr J. 2005. ADP-ribose-1"-
764 monophosphatase: a conserved coronavirus enzyme that is dispensable for viral replication
765 in tissue culture. J Virol 79:12721-31.
766 32. Grunewald ME, Chen Y, Kuny C, Maejima T, Lease R, Ferraris D, Aikawa M, Sullivan
767 CS, Perlman S, Fehr AR. 2019. The coronavirus macrodomain is required to prevent
768 PARP-mediated inhibition of virus replication and enhancement of IFN expression. PLoS
769 Pathog 15:e1007756.
770 33. Kerr CM, Parthasarathy S, Schwarting N, O'Connor JJ, Pfannenstiel JJ, Giri E, More S,
771 Orozco RC, Fehr AR. 2023. PARP12 is required to repress the replication of a Mac1 mutant
772 coronavirus in a cell- and tissue-specific manner. J Virol 97:e0088523.
773 34. Voth LS, O'Connor JJ, Kerr CM, Doerger E, Schwarting N, Sperstad P, Johnson DK, Fehr
774 AR. 2021. Unique Mutations in the Murine Hepatitis Virus Macrodomain Differentially
775 Attenuate Virus Replication, Indicating Multiple Roles for the Macrodomain in
776 Coronavirus Replication. J Virol 95:e0076621.
777 35. Hammond RG, Schormann N, McPherson RL, Leung AKL, Deivanayagam CCS, Johnson
778 MA. 2021. ADP-ribose and analogues bound to the deMARylating macrodomain from the
779 bat coronavirus HKU4. Proc Natl Acad Sci U S A 118.
780 36. Karras GI, Kustatscher G, Buhecha HR, Allen MD, Pugieux C, Sait F, Bycroft M, Ladurner
781 AG. 2005. The macro domain is an ADP-ribose binding module. EMBO J 24:1911-20.
782 37. Neuvonen M, Ahola T. 2009. Differential activities of cellular and viral macro domain
783 proteins in binding of ADP-ribose metabolites. J Mol Biol 385:212-25.
784 38. Roy A, Alhammad YM, McDonald P, Johnson DK, Zhuo J, Wazir S, Ferraris D, Lehtio L,
785 Leung AKL, Fehr AR. 2022. Discovery of compounds that inhibit SARS-CoV-2 Mac1-
786 ADP-ribose binding by high-throughput screening. Antiviral Res 203:105344.
787 39. Schuller M, Riedel K, Gibbs-Seymour I, Uth K, Sieg C, Gehring AP, Ahel I, Bracher F,
788 Kessler BM, Elkins JM, Knapp S. 2017. Discovery of a Selective Allosteric Inhibitor
789 Targeting Macrodomain 2 of Polyadenosine-Diphosphate-Ribose Polymerase 14. ACS
790 Chem Biol 12:2866-2874.
791 40. Ekblad T, Verheugd P, Lindgren AE, Nyman T, Elofsson M, Schuler H. 2018. Identification
792 of Poly(ADP-Ribose) Polymerase Macrodomain Inhibitors Using an AlphaScreen
793 Protocol. SLAS Discov 23:353-362.
794 41. Fehr AR. 2020. Bacterial Artificial Chromosome-Based Lambda Red Recombination with
795 the I-SceI Homing Endonuclease for Genetic Alteration of MERS-CoV. Methods Mol Biol
796 2099:53-68.

797 42. Li K, Wohlford-Lenane CL, Channappanavar R, Park JE, Earnest JT, Bair TB, Bates AM,
798 Brogden KA, Flaherty HA, Gallagher T, Meyerholz DK, Perlman S, McCray PB, Jr. 2017.
799 Mouse-adapted MERS coronavirus causes lethal lung disease in human DPP4 knockin
800 mice. Proc Natl Acad Sci U S A 114:E3119-E3128.
801 43. Makrynitsa GI, Ntonti D, Marousis KD, Birkou M, Matsoukas MT, Asami S, Bentrop D,
802 Papageorgiou N, Canard B, Coutard B, Spyroulias GA. 2019. Conformational plasticity of
803 the VEEV macro domain is important for binding of ADP-ribose. J Struct Biol 206:119-
804 127.
805 44. Hoch NC. 2021. Host ADP-ribosylation and the SARS-CoV-2 macrodomain. Biochem Soc
806 Trans 49:1711-1721.
807 45. Eckei L, Krieg S, Butepage M, Lehmann A, Gross A, Lippok B, Grimm AR, Kummerer
808 BM, Rossetti G, Luscher B, Verheugd P. 2017. The conserved macrodomains of the non-
809 structural proteins of Chikungunya virus and other pathogenic positive strand RNA viruses
810 function as mono-ADP-ribosylhydrolases. Sci Rep 7:41746.
811 46. Schuller M, Correy GJ, Gahbauer S, Fearon D, Wu T, Diaz RE, Young ID, Carvalho
812 Martins L, Smith DH, Schulze-Gahmen U, Owens TW, Deshpande I, Merz GE, Thwin AC,
813 Biel JT, Peters JK, Moritz M, Herrera N, Kratochvil HT, Consortium QSB, Aimon A,
814 Bennett JM, Brandao Neto J, Cohen AE, Dias A, Douangamath A, Dunnett L, Fedorov O,
815 Ferla MP, Fuchs MR, Gorrie-Stone TJ, Holton JM, Johnson MG, Krojer T, Meigs G, Powell
816 AJ, Rack JGM, Rangel VL, Russi S, Skyner RE, Smith CA, Soares AS, Wierman JL, Zhu
817 K, O'Brien P, Jura N, Ashworth A, Irwin JJ, Thompson MC, Gestwicki JE, et al. 2021.
818 Fragment binding to the Nsp3 macrodomain of SARS-CoV-2 identified through
819 crystallographic screening and computational docking. Sci Adv 7.
820 47. Deng X, Mettelman RC, O'Brien A, Thompson JA, O'Brien TE, Baker SC. 2019. Analysis
821 of Coronavirus Temperature-Sensitive Mutants Reveals an Interplay between the
822 Macrodomain and Papain-Like Protease Impacting Replication and Pathogenesis. J Virol
823 93.
824 48. Chea C, Lee DY, Kato J, Ishiwata-Endo H, Moss J. 2023. Macrodomain Mac1 of SARS-
825 CoV-2 Nonstructural Protein 3 Hydrolyzes Diverse ADP-ribosylated Substrates. bioRxiv
826 doi:10.1101/2023.02.07.527501.
827 49. Heer CD, Sanderson DJ, Voth LS, Alhammad YMO, Schmidt MS, Trammell SAJ, Perlman
828 S, Cohen MS, Fehr AR, Brenner C. 2020. Coronavirus infection and PARP expression
829 dysregulate the NAD metabolome: An actionable component of innate immunity. J Biol
830 Chem 295:17986-17996.
831 50. Izadpanah A, Mudd JC, Garcia JGN, Srivastav S, Abdel-Mohsen M, Palmer C, Goldman
832 AR, Kolls JK, Qin X, Rappaport J. 2023. SARS-CoV-2 infection dysregulates NAD
833 metabolism. Front Immunol 14:1158455.
834 51. Jiang Y, Deng Y, Pang H, Ma T, Ye Q, Chen Q, Chen H, Hu Z, Qin CF, Xu Z. 2022.
835 Treatment of SARS-CoV-2-induced pneumonia with NAD(+) and NMN in two mouse
836 models. Cell Discov 8:38.
837 52. Jankevicius G, Hassler M, Golia B, Rybin V, Zacharias M, Timinszky G, Ladurner AG.
838 2013. A family of macrodomain proteins reverses cellular mono-ADP-ribosylation. Nat
839 Struct Mol Biol 20:508-14.
840 53. Van Der Spoel D, Lindahl E, Hess B, Groenhof G, Mark AE, Berendsen HJ. 2005.
841 GROMACS: fast, flexible, and free. J Comput Chem 26:1701-18.

842 54. Michalska K, Kim Y, Jedrzejczak R, Maltseva NI, Stols L, Endres M, Joachimiak A. 2020.
843 Crystal structures of SARS-CoV-2 ADP-ribose phosphatase: from the apo form to ligand
844 complexes. IUCrJ 7:814-824.
845 55. Jo S, Kim T, Iyer VG, Im W. 2008. CHARMM-GUI: a web-based graphical user interface
846 for CHARMM. J Comput Chem 29:1859-65.
847 56. Roy Wong LY, Zheng J, Wilhelmsen K, Li K, Ortiz ME, Schnicker NJ, Pezzulo AA,
848 Szachowicz PJ, Klumpp K, Aswad F, Rebo J, Narumiya S, Murakami M, Meyerholz DK,
849 Fortney K, McCray PB, Perlman S. 2021. Eicosanoid signaling as a therapeutic target in
850 middle-aged mice with severe COVID-19. bioRxiv doi:10.1101/2021.04.20.440676.
851 57. Almazan F, DeDiego ML, Sola I, Zuniga S, Nieto-Torres JL, Marquez-Jurado S, Andres
852 G, Enjuanes L. 2013. Engineering a replication-competent, propagation-defective Middle
853 East respiratory syndrome coronavirus as a vaccine candidate. mBio 4:e00650-13.
854 58. Li K, Li Z, Wohlford-Lenane C, Meyerholz DK, Channappanavar R, An D, Perlman S,
855 McCray PB, Jr., He B. 2020. Single-Dose, Intranasal Immunization with Recombinant
856 Parainfluenza Virus 5 Expressing Middle East Respiratory Syndrome Coronavirus (MERS-
857 CoV) Spike Protein Protects Mice from Fatal MERS-CoV Infection. mBio 11.
858

859 **FIGURE LEGENDS**

860 **Figure 1. The GIF motif in loop 2 of Mac1 is highly conserved and is closely associated with**
861 **both phosphate groups and the terminal ribose of ADP-ribose.** (A) Sequence alignment of
862 Mac1 across viral and human macrodomains. The GIF motif is boxed in Red. (B) Overlay of the
863 SARS-CoV-2 (purple) (6WOJ) and MERS-CoV (teal) (5HOL) Mac1 ADP-ribose binding domains
864 with ADP-ribose (7), highlighting the GIF motif and conserved asparagine and aspartic acid
865 residues discussed in the manuscript.

866 **Figure 2. MHV F1441A mutation is attenuated in cell lines and in primary cells.** DBTs (A),
867 L929s (B), and M2 macrophages (C) were infected with JHMV at an MOI of 0.1 PFU/cell. Cells
868 and supernatants were collected at indicated times and assayed for progeny infectious virus by
869 plaque assay. The data in each panel show one experiment representative of three independent
870 experiments with n = 3 for each experiment.

871 **Figure 3. MHV F1441A, but not I1440A, is partially attenuated in *in vivo*.** (A-C) Male and
872 female C57BL/6 mice were infected intranasally with WT, I1440A, and F1441A JHMV at 1×10^4
873 PFU. Mice were monitored for survival (A), weight loss (B), and disease score (as described in
874 Methods) (C) for 12 days post-infection (dpi). WT, n=4 mice; IA, n=8 mice; FA, n=8 mice. (D)
875 Brains were collected at 5 dpi and titers were determined by plaque assay. WT, n=6; IA, n=7; FA,
876 n=8. The data show the combined results from two independent experiments.

877 **Figure 4. MERS-CoV I238A and F1239A Mac1 mutations have opposing effects on ADP-**
878 **ribose binding and hydrolysis.** (A) Mac1 protein was incubated with free ADP-ribose and
879 binding affinity was measured by isothermal calorimetry as described in Methods. (B) An ADP-
880 ribosylated peptide was incubated with indicated macrodomains at increasing concentrations and
881 Alphacounts were measured as described in Methods. (C) ADP-ribose (ADPr) competition assays

882 were used to block the interaction between macrodomain proteins and ADP-ribosylation peptides
883 in the AS assay. Data was analyzed as described in Methods. The data in A-C represent combined
884 results of 2 independent experiments for each protein. (D) WT, I1153A, and F1154A MERS-CoV
885 Mac1 proteins were incubated with MARylated PARP10 CD *in vitro* at an [E]/[S] molar ratio of
886 1:5 for the indicated times at 37°C. ADP-ribosylated PARP10 CD was detected by IB with anti-
887 ADP- ribose binding reagent (MAB1076; MilliporeSigma) while total PARP10 CD protein levels
888 was detected by IB with GST antibody. The reaction with PARP10 CD incubated alone at 37°C
889 was stopped at 0 or 30 min. The image in D is representative of 2 independent experiments. (E)
890 The level of de-MARylation was measured after 30 minutes by quantifying relative band intensity
891 (ADP-ribose/GST-PARP10) using ImageJ software. Error bars represent standard deviations. The
892 results in E are the combined resulted of 2 independent experiments.

893 **Figure 5. MERS-CoV I1238A and F1239A have similarly decreased replication in Calu-3**
894 **cells.** (A-B) Vero81 (A) and Calu3 (B) cells were infected at an MOI of 0.1 PFU/cell. Cells and
895 supernatants were collected at indicated times post-infection (hpi) and progeny virus was measured
896 by plaque assay. The data in panels A and B show one experiment representative of two (A) or
897 three (B) independent experiments with n = 3 for each experiment.

898 **Figure 6. SARS-CoV-2 Mac1 mutations impact both ADP-ribose binding and hydrolysis.** (A)
899 SARS-CoV-2 Mac1 protein was incubated with free ADP-ribose and binding affinity was
900 measured by isothermal calorimetry as described in Methods. (B) WT, I1153A, and F1154A Mac1
901 proteins (10 μM) were incubated with increasing concentrations of ADP-ribose and measured by
902 DSF as described in Methods. The data in panels A and B show one experiment representative of
903 three independent experiments. (C) A control (non-ADP-ribosylated) peptide was incubated with
904 indicated Mac1 proteins at increasing concentrations and Alphacounts were measured as described

905 in Methods. (D) An ADP-ribosylated peptide (same peptide sequence as in (C)) was incubated
906 with indicated Mac1 proteins at increasing concentrations and Alphacounts were measured as
907 described in Methods. The data in panels C and D show one experiment representative of two
908 independent experiments. (E) WT, I1153A, and F1154A SARS-CoV-2 Mac1 proteins were
909 incubated with MARylated PARP10 CD *in vitro* at an [E]/[S] molar ratio of 1:5 for the indicated
910 times at 37°C. ADP-ribosylated PARP10 CD was detected by IB with anti-ADP- ribose binding
911 reagent (MAB1076; MilliporeSigma) while total PARP10 CD protein levels were detected by IB
912 with GST antibody. The reaction with PARP10 CD incubated alone at 37°C was stopped at 0 or
913 30 min. The data in panels D shows one experiment representative of three independent
914 experiments. (F) The level of de-MARylation from 3 separate experiments was measured by
915 quantifying relative band intensity (ADP-ribose/GST-PARP10) using ImageJ software. Intensity
916 values were plotted and fitted to a nonlinear regression curve; error bars represent standard
917 deviations. (G) ADP-ribosylated peptide was incubated with WT and N1062A Mac1 proteins at
918 increasing concentrations and Alphacounts were measured as described in Methods. (H) ADP-
919 ribose (ADPr) competition assays were used to block the interaction between WT and N1062A
920 Mac1 proteins and ADP-ribosylated peptides. Data was analyzed as described in Methods. The
921 data represent the means ± SD of 2 independent experiments for each protein. (I) WT and N1062A
922 Mac1 proteins (10 μM) were incubated with increasing concentrations of ADP-ribose and
923 measured by DSF as described in Methods. (J) WT and N1062A SARS-CoV-2 Mac1 proteins were
924 incubated with MARylated PARP10 CD *in vitro* at an [E]/[S] molar ratio of 1:5 for the indicated
925 times at 37°C. ADP-ribosylated PARP10 CD was detected by IB with anti-ADP-ribose binding
926 reagent (green) while total PARP10 CD protein levels were detected by IB with GST antibody
927 (red). The reaction with PARP10 CD incubated alone at 37°C was stopped at 0 or 30 min. The data

928 is representative of 2 independent experiments. (K) The level of de-MARylation in D was
929 measured by quantifying relative band intensity from 2 independent experiments (ADP-
930 ribose/GST-PARP10) using ImageJ software. Intensity values were plotted and fitted to a nonlinear
931 regression curve. The data represent the means ± SD of 2 independent experiments for each
932 protein.

933 **Figure 7. SARS-CoV-2 Mac1 I1153A and F1154A mutations have detrimental effects on**
934 **SARS-CoV-2 replication in the presence of IFNγ.** Calu-3 (A) and A549-ACE2 (B) cells were
935 pretreated with 500 units of IFNγ for 18-20 hours prior to infection. Then cells were infected at an
936 MOI of 0.1 PFU/cell. Cells and supernatants were collected at 48 hpi and progeny virus was
937 measured by plaque assay. The data in panels A and B show one experiment representative of three
938 independent experiments with $n = 3$ for each experiment.

939 **Figure 8. SARS-CoV-2 I1153A and F1154A are highly attenuated and induce elevated innate**
940 **immune responses in the lungs of infected mice.** K18-ACE2 C57BL/6 mice were infected i.n.
941 with 2.5 x 10^4 PFU of virus. (A-B) Survival (A) and weight loss (B) were monitored for 14 days.
942 n=5 for survival and n=9 for weightloss for all groups. (C) Lungs were harvested at 1 dpi and viral
943 titers were determined by plaque assay. n=6 for all groups. (D) Lungs were harvested at 8 dpi and
944 viral titers were determined by plaque assay. Dotted line indicates limit of detection. n=3 for WT,
945 n=4 for I1153A and F1154A. (E) Photomicrographs (hematoxylin and eosin stain) of lungs
946 infected mice at 8 dpi demonstrating bronchointerstitial pneumonia (black arrow) and edema and
947 fibrin (open arrow). (F) Mice were scored for bronchointerstitial pneumonia, inflammation, and
948 edema/fibrin deposition (each on a 0-5 scale). Bar graphs represent cumulative lung pathology
949 score in WT n=3, I1153A n=4, F1154A n=4. (G) Lungs were harvested at 1 dpi in Trizol and RNA

950 was isolated. Transcripts levels were determined using qPCR with the ΔCT method. n=6 for all
951 groups.

952 **Figure 9. Models of isoleucine-to-alanine mutation on Mac1 structure and virus replication.**
953 (A) Molecular simulation of the ADP-ribose binding domain of the SARS-CoV-2 Mac1 protein
954 was performed in absence and presence of ADP-ribose. The 1 ns averaged I/A1153 to G1069
955 distance was measured through the course of four 25 ns MD simulations of ADP-ribose bound and
956 unbound WT and I1153A protein. (B-C) A representative image at 12 ns of the simulation
957 demonstrating the distance between the I1153 and A1153 residues and G1069 at 12 ns into the
958 simulation without ADP-ribose in a space-filling (B) or stick model (C). (D) (Left) In the presence
959 of IFNγ, the WT SARS-CoV-2 Mac1 removes ADP-ribose from specific proteins (red and blue)
960 that have an ADP-ribose on an acidic reside which enhances virus replication. (Right) Due to the
961 open conformation of SARS-CoV-2 I1153A Mac1 protein, it binds to ADP-ribose bound to non-
962 acidic residues (gold and green). Since Mac1 cannot remove proteins from non-acidic residues,
963 this limits its ability to interact with relevant substrate, and the ADP-ribose remains on its normal
964 target proteins leading to poor virus replication.

965 **Table 1.** Summary of Mac1 ADP-ribose binding, hydrolysis, and replication activity

Virus	MERS-CoV				SARS-CoV-2			
Mutation	WT	N1147A	I1238A**	F1239A	WT	N1062A*	I1153A	F1154A
Binding	+	nd	+/++	-	+	+	++	++
Hydrolysis*	+	nd	+	-	+	-	+	-
Replication***	+	-	-	-	+	-	-	-

966 nd, not determined
967 (+) - WT levels
968 (++) - significantly increased compared to WT
969 (-) - significantly decreased compared to WT
970 *SARS-CoV-2 N1062A binding and hydrolysis was not directly compared with I1153A and
971 F1154A
972 ** MERS-CoV I1238A binding results depend on the assay
973 ***SARS-CoV-2 replication is defined in the presence of IFNγ

974 **Table 2. Primers for generating recombinant CoV BACs**

Viral Strain	Forward 5'-3'	Reverse 5'-3'
MHV-CoV		
N1347A	TTTGCGCAGAGTTGGTGCTGAAGTCATCGTCAACCCTGCT GCTGGGCGCATGGCTCATGGaggatgacgacgataagtaggg	TAGCACCTGCAACACCCGCACCATGAGCCATGCGCCCAGCAGCAGGGTTGACG ATGACTTgccagtgttacaaccaattaacc
I1440A	TAAGTGTGACAATGTTGTCACCACTTTAATTTCGGCTGGTG CATTTAGTGTGCCTACTGAaggatgacgacgataagtaggg	CAAGTAGATAAGTTAAGGAAACATCAGTAGGCACACTAAATGCACCA GCCGAAATTAAAGgccagtgttacaaccaattaacc
F1441A	GTGTGACAATGTTGTCACCACTTTAATTTCGGCTGGTATAG CTAGTGTGCCTACTGATGTaggatgacgacgataagtaggg	CAAGTAGATAAGTTAAGGAAACATCAGTAGGCACACTAGCTATACCA GCCGAAATTAAAGgccagtgttacaaccaattaacc
SARS-CoV-2		
N1062A	TAAAAAGGTAAAACCAACAGTGGTTGTTAATGCAGCCGCT GTTTACCTTAAACATGGAGGaggatgacgacgataagtaggg	TTAAGGCTCCTGCAACACCTCCTCCATGTTTAAGGTAAACAGCGGCT GCATTAACAACCAgccagtgttacaaccaattaacc
I1153A	GCACGAAGTTCTACTTGCACCATTATTATCAGCTGGTGCTT TTGGTGCTGACCCTATACAaggatgacgacgataagtaggg	CTACACAAACTCTTAAAGAATGTATAGGGTCAGCACCAAAAGCACCA GCTGATAATAATGgccagtgttacaaccaattaacc
F1154A	CGAAGTTCTACTTGCACCATTATTATCAGCTGGTATTGCTG GTGCTGACCCTATACATTCaggatgacgacgataagtaggg	TATCTACACAAACTCTTAAAGAATGTATAGGGTCAGCACCAGCAATAC CAGCTGATAATAgccagtgttacaaccaattaacc
MERS-CoV.MA		
GFP	AAATTGTTCATTCTTATCCCATTTTACATCATCCAGGATTTT AACGAACTatggtgagcaagggcgagga	ACTAATGGATTAGCCTCTACACGGGACCCATAGTAGCGCAGAGCTGC TTActtgtacagctcgtccatgc
N1147A	AGCCAAGTGCTATGGGGAGTCTGTGTTAGTTAATGCTGCT GCCACACATCTTAAGCATGGaggatgacgacgataagtaggg	TAGCACCAGCGATACCACCGCCATGCTTAAGATGTGTGGCAGCAGCA TTAACTAACACAGgccagtgttacaaccaattaacc
I1238A	GCATATCCTCTTGTAGTCACTCCTCTTGTTTCAGCAGGCG CATTTGGTGTAAAACCAGCTaggatgacgacgataagtaggg	AATAAGATAATCAAAAGACACAGCTGGTTTTACACCAAATGCGCCTGC TGAAACAAGAGgccagtgttacaaccaattaacc
F1239A	ATATCCTCTTGTAGTCACTCCTCTTGTTTCAGCAGGCATAG CTGGTGTAAAACCAGCTGTaggatgacgacgataagtaggg	TCCCTAATAAGATAATCAAAAGACACAGCTGGTTTTACACCAGCTATG CCTGCTGAAACAgccagtgttacaaccaattaacc

975 Viral sequences are indicated in uppercase; marker sequences are indicated in lowercase.

A

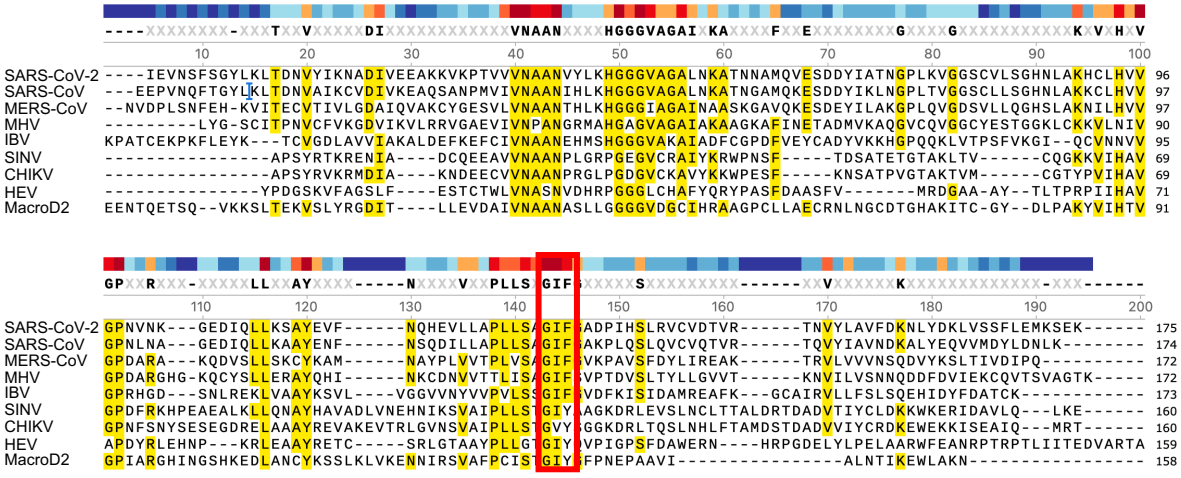

B

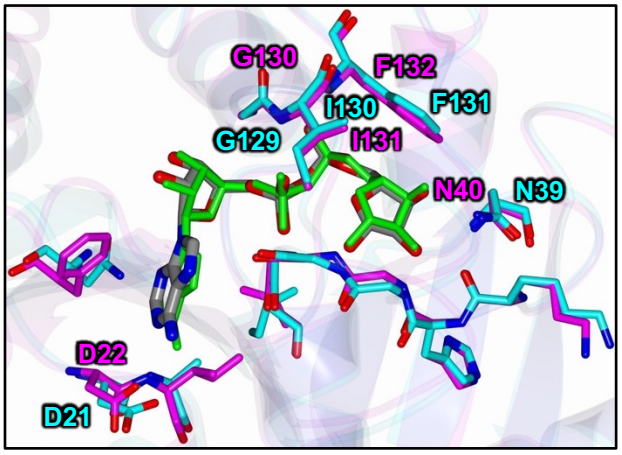

Figure 1. The GIF motif in loop 2 of Mac1 is highly conserved and is closely associated with both phosphate groups and the terminal ribose of ADP-ribose. (A) Sequence alignment of Mac1 across viral and human macrodomains. GIF motif is boxed in Red. (B) Overlay of the SARS-CoV-2 (purple) (6WOJ) and MERS-CoV (teal) (5HOL) Mac1 ADP-ribose binding domains with ADP-ribose, highlighting the GIF motif and conserved asparagine and aspartic acid residues discussed in the manuscript.

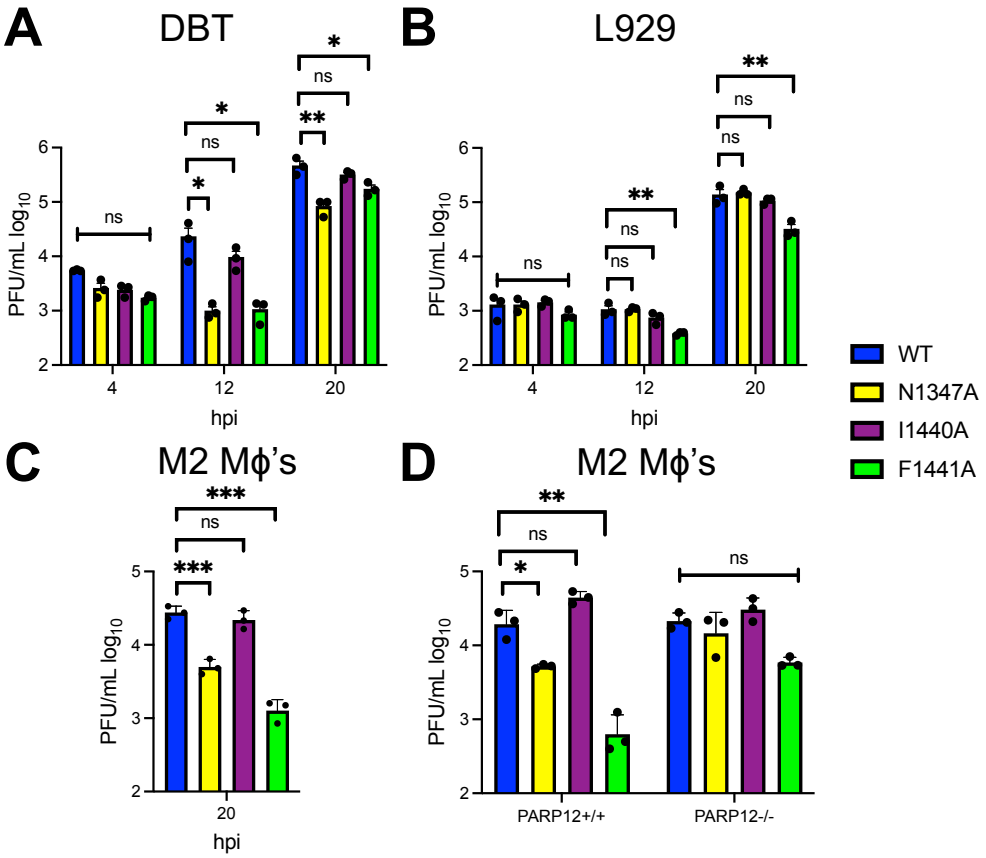

Figure 2. MHV F1441A mutation is attenuated in cell lines and in primary cells. DBTs (A), L929s (B), and M2 macrophages (C-D) were infected with JHMV at an MOI of 0.1 PFU/cell. Cells and supernatants were collected at indicated times and assayed for progeny infectious virus by plaque assay. The data in each panel show one experiment representative of three independent experiments with n = 3 for each experiment.

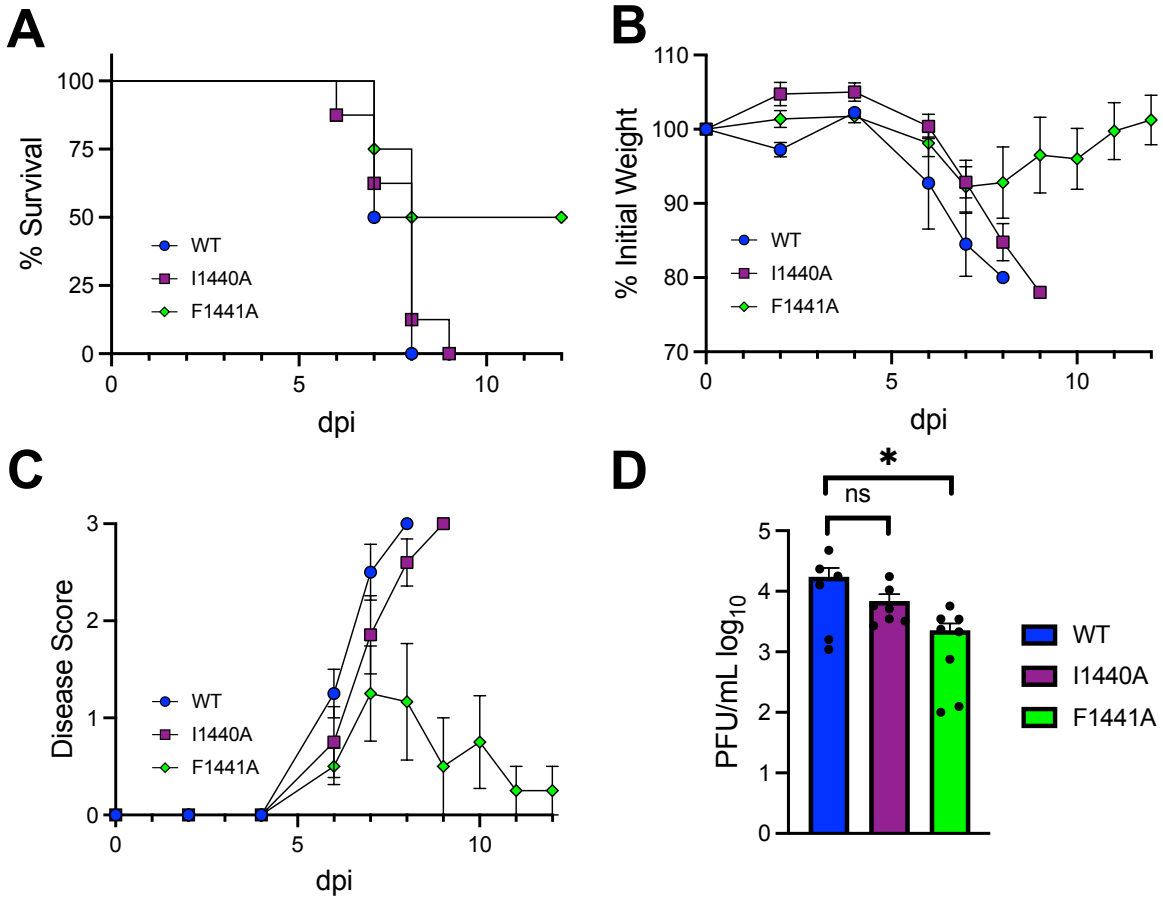

Figure 3. MHV F1441A, but not I1440A, is partially attenuated in *in vivo*. (A-C) Male and female C57BL/6 mice were infected intranasally with WT, I1440A, and F1441A JHMV at 1 X 10^4 PFU. Mice were monitored for survival (A), weight loss (B), and disease score (as described in Methods) (C) for 12 days post-infection (dpi). WT, n=4 mice; IA, n=8 mice; FA, n=8 mice. (D) Brains were collected at 5 dpi and titers were determined by plaque assay. WT, n=6; IA, n=7; FA, n=8. The data show the combined results from two independent experiments.

A

Mac1	Kd (μM)	ΔH (kcalmol^{-1})	ΔG (kcalmol^{-1})	-TΔS (kcalmol^{-1})
MERS-CoV - WT	7.2 ± 0.19	-46 ± 0.7	-29 ± 0.07	16 ± 0.6
I1238A	12.7 ± 0.21	-34 ± 1	-28 ± 0.1	6.4 ± 1
F1239A	60 ± 5	-38 ± 11	-24 ± 0.2	5 ± 1

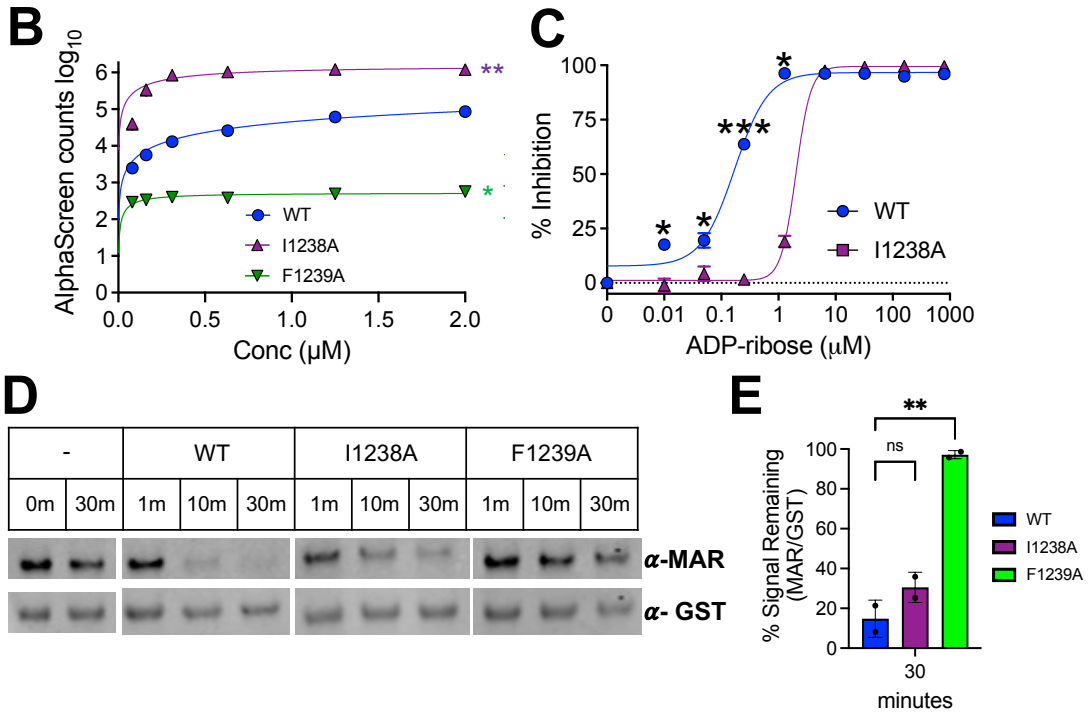

Figure 4. MERS-CoV I238A and F1239A Mac1 mutations have opposing effects on ADP-ribose binding and hydrolysis. (A) Mac1 protein was incubated with free ADP-ribose and binding affinity was measured by isothermal calorimetry as described in Methods. (B) An ADP-ribosylated peptide was incubated with indicated macrodomains at increasing concentrations and Alphacounts were measured as described in Methods. (C) ADP-ribose (ADPr) competition assays were used to block the interaction between macrodomain proteins and ADP-ribosylation peptides in the AS assay. Data was analyzed as described in Methods. The data in A-C represent combined results of 2 independent experiments for each protein. (D) WT, I1153A, and F1154A MERS-CoV Mac1 proteins were incubated with MARylated PARP10 CD in vitro at an [E]/[S] molar ratio of 1:5 for the indicated times at 37°C. ADP-ribosylated PARP10 CD was detected by IB with anti-ADP- ribose binding reagent (MAB1076; MilliporeSigma) while total PARP10 CD protein levels was detected by IB with GST antibody. The reaction with PARP10 CD incubated alone at 37°C was stopped at 0 or 30 min. The image in D is representative of 2 independent experiments. (E) The level of de-MARylation was measured after 30 minutes by quantifying relative band intensity (ADP-ribose/GST-PARP10) using ImageJ software. Error bars represent standard deviations (SD). The results in E are the combined resulted of 2 independent experiments.

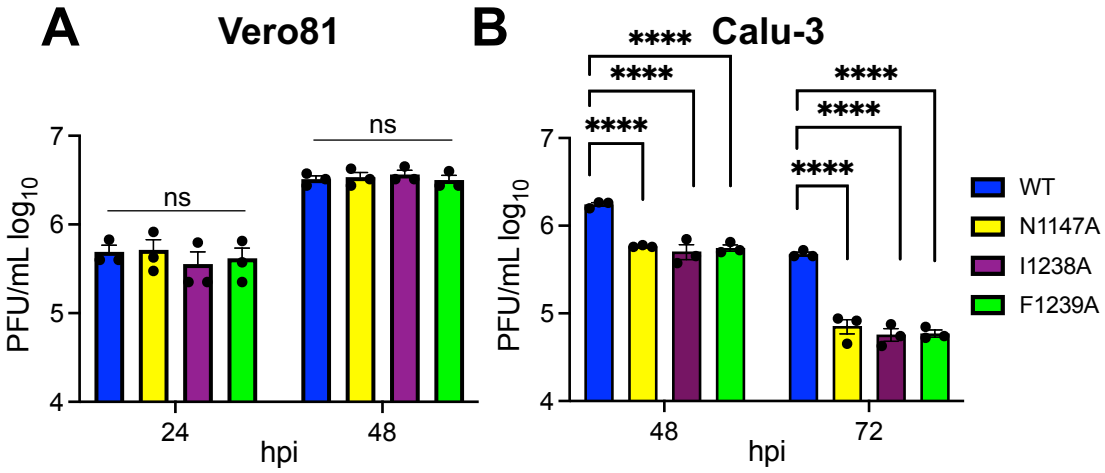

Figure 5. MERS-CoV I1238A and F1239A have similarly decreased replication in human and bat cell lines. (A-C) Vero81 (A) and Calu-3 (B) cells were infected at an MOI of 0.1 PFU/cell. Cells and supernatants were collected at indicated times post-infection (hpi) and progeny virus was measured by plaque assay. The data in panels A, B, and C show one experiment representative of 2 (A) or 3 (B) independent experiments with n = 3 for each experiment.

A

Mac1	Kd (μM)	ΔH (kcalmol^{-1})	ΔG (kcalmol^{-1})	-TΔS (kcalmol^{-1})
SARS-CoV-2 - WT	16.8 ± 0.42	-28 ± 0.07	-27.3 ± 0.07	0.5 ± 0.01
I1153A	5.49 ± 0.09	-7.69 ± 0.78	-7.18 ± 0.01	0.51 ± 0.78
F1154A	5.11 ± 0.21	-6.95 ± 0.65	-7.22 ± 0.03	-0.27 ± 0.67

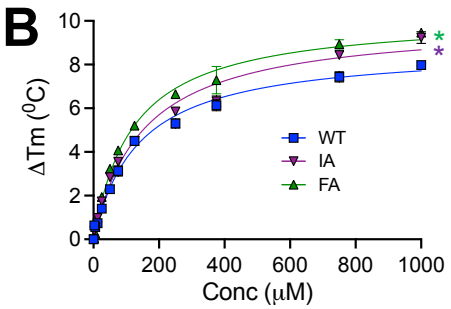

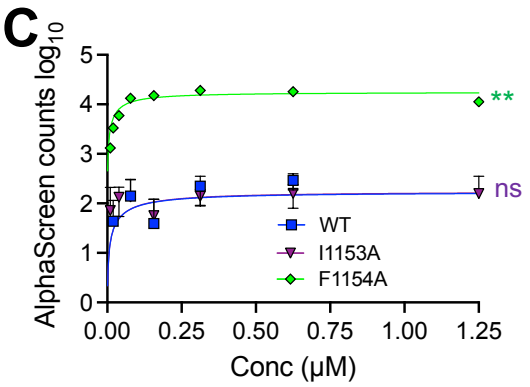

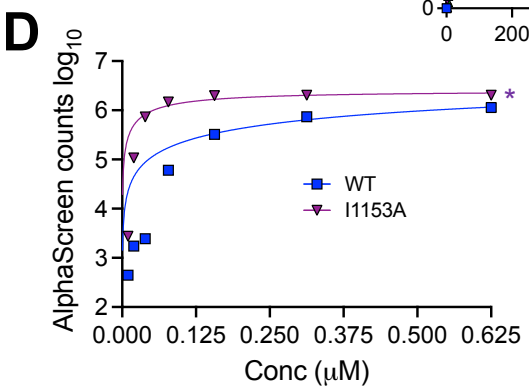

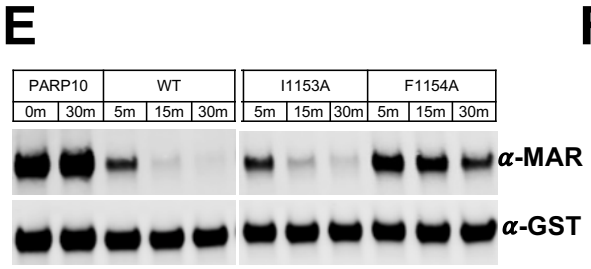

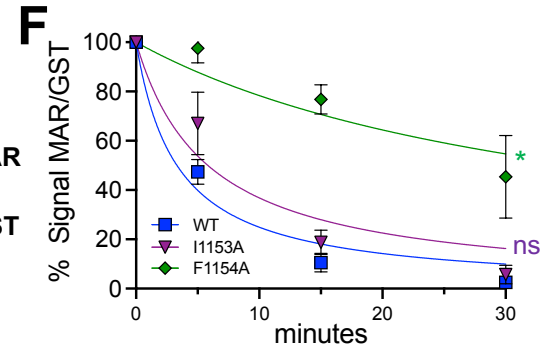

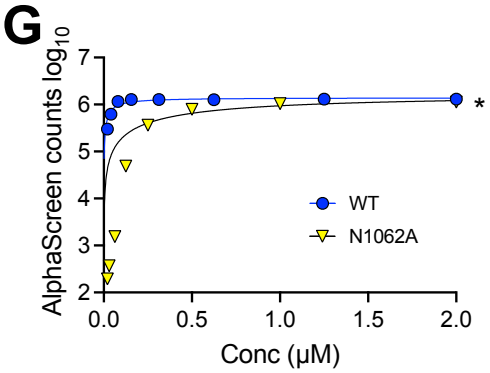

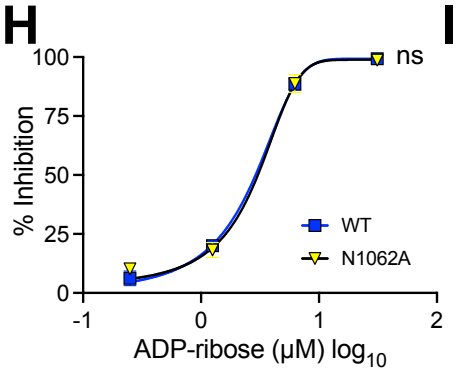

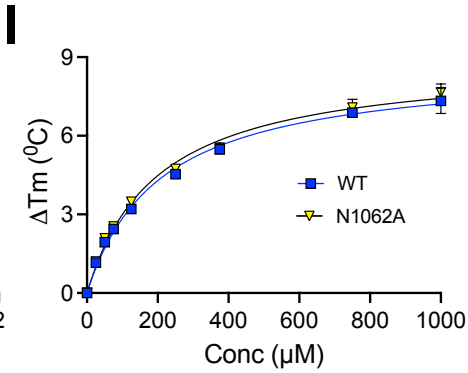

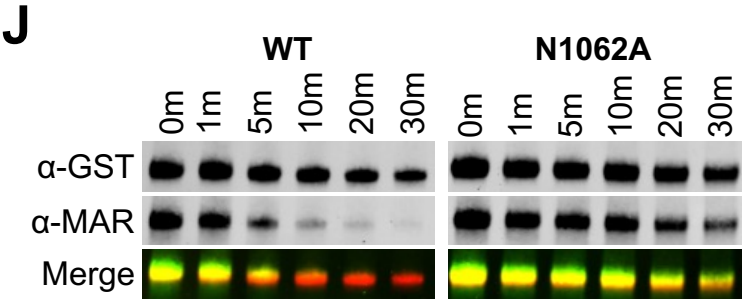

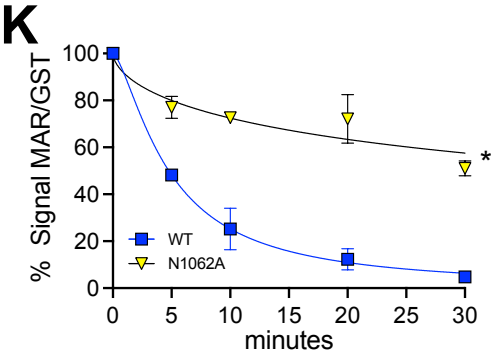

Figure 6. SARS-CoV-2 Mac1 mutations impact both ADP-ribose binding and hydrolysis. (A) SARS-CoV-2 Mac1 protein was incubated with free ADP-ribose and binding affinity was measured by isothermal calorimetry as described in Methods. (B) WT, I1153A, and F1154A Mac1 proteins (10 μM) were incubated with increasing concentrations of ADP-ribose and measured by DSF as described in Methods. The data in panels A and B show one experiment representative of three independent experiments. (C) A control (non-ADP-ribosylated) peptide was incubated with indicated Mac1 proteins at increasing concentrations and Alphacounts were measured as described in Methods. (D) An ADP-ribosylated peptide (same peptide sequence as in (C)) was incubated with indicated Mac1 proteins at increasing concentrations and Alphacounts were measured as described in Methods. The data in panels C and D show one experiment representative of two independent experiments. (E) WT, I1153A, and F1154A SARS-CoV-2 Mac1 proteins were incubated with MARylated PARP10 CD *in vitro* at an [E]/[S] molar ratio of 1:5 for the indicated times at 37°C. ADP-ribosylated PARP10 CD was detected by IB with anti-ADP- ribose binding reagent (MAB1076; MilliporeSigma) while total PARP10 CD protein levels were detected by IB with GST antibody. The reaction with PARP10 CD incubated alone at 37°C was stopped at 0 or 30 min. The data in panels D shows one experiment representative of three independent experiments. (F) The level of de-MARylation from 3 separate experiments was measured by quantifying relative band intensity (ADP-ribose/GST-PARP10) using ImageJ software. Intensity values were plotted and fitted to a nonlinear regression curve; error bars represent standard deviations. (G) ADP-ribosylated peptide was incubated with WT and N1062A Mac1 proteins at increasing concentrations and Alphacounts were measured as described in Methods. (H) ADP-ribose (ADPr) competition assays were used to block the interaction between WT and N1062A Mac1 proteins and ADP-ribosylated peptides. Data was analyzed as described in Methods. The data represent the means ± SD of 2 independent experiments for each protein. (I) WT and N1062A Mac1 proteins (10 μM) were incubated with increasing concentrations of ADP-ribose and measured by DSF as described in Methods. (J) WT and N1062A SARS-CoV-2 Mac1 proteins were incubated with MARylated PARP10 CD *in vitro* at an [E]/[S] molar ratio of 1:5 for the indicated times at 37°C. ADP-ribosylated PARP10 CD was detected by IB with anti-ADP-ribose binding reagent (green) while total PARP10 CD protein levels were detected by IB with GST antibody (red). The reaction with PARP10 CD incubated alone at 37°C was stopped at 0 or 30 min. The data is representative of 2 independent experiments. (K) The level of de-MARylation in D was measured by quantifying relative band intensity from 2 independent experiments (ADP-ribose/GST-PARP10) using ImageJ software. Intensity values were plotted and fitted to a nonlinear regression curve. The data represent the means ± SD of 2 independent experiments for each protein.

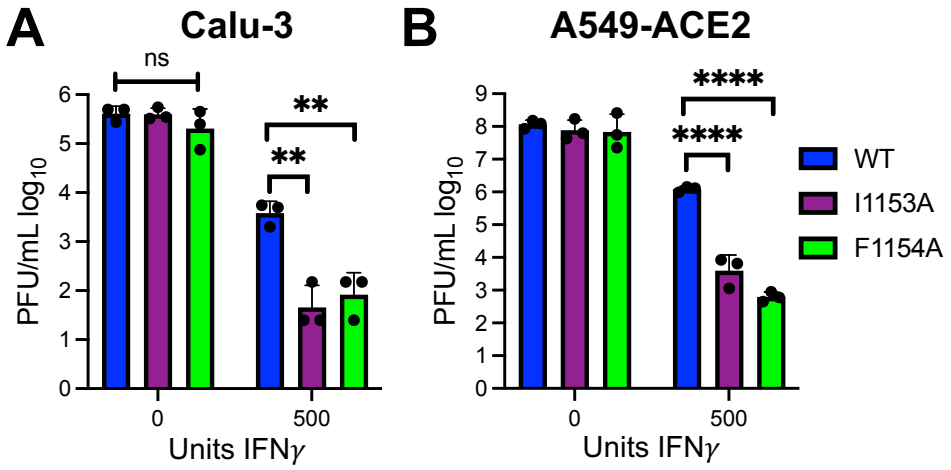

Figure 7. SARS-CoV-2 Mac1 I1153A and F1154A mutations have detrimental effects on SARS-CoV-2 replication in the presence of IFNγ. Calu-3 (A) and A549-ACE2 (B) cells were pretreated with 500 units of IFNγ for 18-20 hours prior to infection. Then cells were infected at an MOI of 0.1 PFU/cell. Cells and supernatants were collected at 48 hpi and progeny virus was measured by plaque assay. The data in panels A and B show one experiment representative of three independent experiments with $n = 3$ for each experiment.

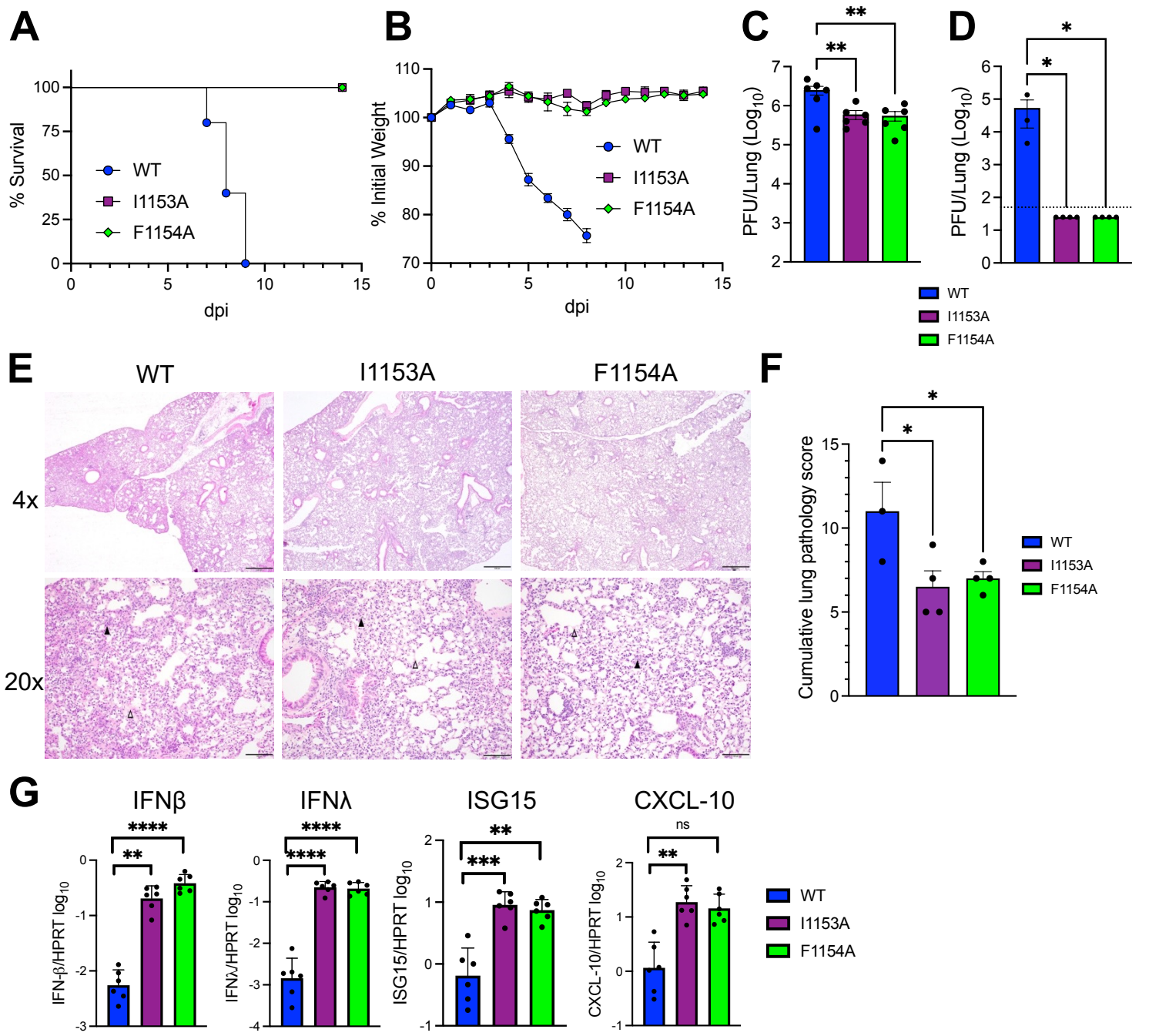

Figure 8. SARS-CoV-2 I1153A and F1154A are highly attenuated and induce elevated innate immune responses in the lungs of infected mice. K18-ACE2 C57BL/6 mice were infected i.n. with 2.5 x 10^4 PFU of virus. (A-B) Survival (A) and weight loss (B) were monitored for 14 days. n=5 for survival and n=9 for weightloss for all groups. (C) Lungs were harvested at 1 dpi and viral titers were determined by plaque assay. n=6 for all groups. (D) Lungs were harvested at 8 dpi and viral titers were determined by plaque assay. Dotted line indicates limit of detection. n=3 for WT, n=4 for I1153A and F1154A. (E) Photomicrographs (hematoxylin and eosin stain) of lungs infected mice at 8 dpi demonstrating bronchointerstitial pneumonia (black arrow) and edema and fibrin (open arrow). (F) Mice were scored for bronchointerstitial pneumonia, inflammation, and edema/fibrin deposition (each on a 0-5 scale). Bar graphs represent cumulative lung pathology score in WT n=3, I1153A n=4, F1154A n=4. (G) Lungs were harvested at 1 dpi in Trizol and RNA was isolated. Transcripts levels were determined using qPCR with the ΔCT method. n=6 for all groups.

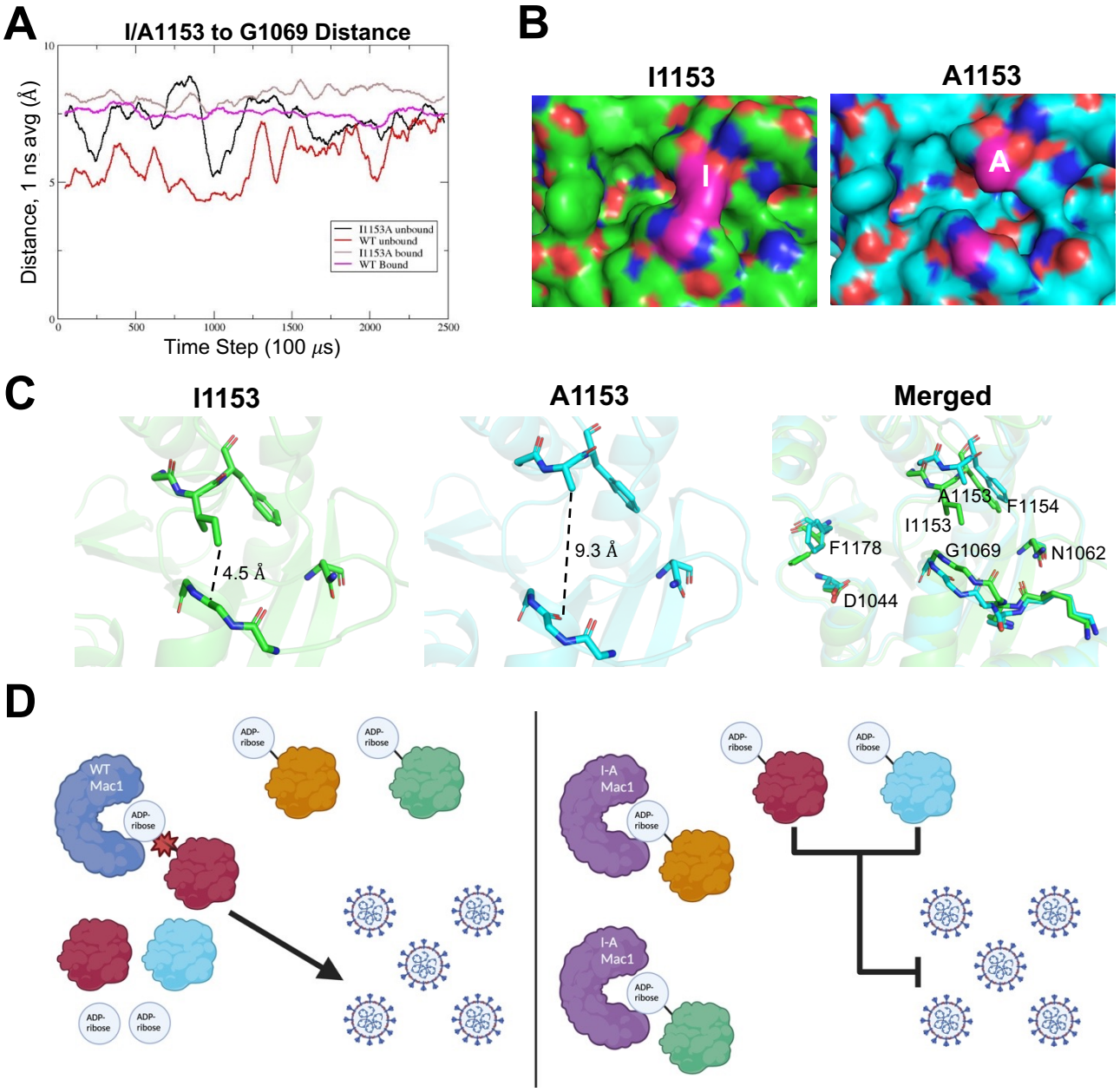

Figure 9. Models of isoleucine-to-alanine mutation on Mac1 structure and virus replication. (A) Molecular simulation of the ADP-ribose binding domain of the SARS-CoV-2 Mac1 protein was performed in absence and presence of ADP-ribose. The 1 ns averaged I/A1153 to G1069 distance was measured through the course of four 25 ns MD simulations of ADP-ribose bound and unbound WT and I1153A protein. (B-C) A representative image at 12 ns of the simulation demonstrating the distance between the I1153 and A1153 residues and G1069 at 12 ns into the simulation without ADP-ribose in a space-filling (B) or stick model (C). (D) (Left) In the presence of IFNγ, the WT SARS-CoV-2 Mac1 removes ADP-ribose from specific proteins (red and blue) that have an ADP-ribose on an acidic reside which enhances virus replication. (Right) Due to the open conformation of SARS-CoV-2 I1153A Mac1 protein, it binds to ADP-ribose bound to non-acidic residues (gold and green). Since Mac1 cannot remove proteins from non-acidic residues, this limits its ability to interact with relevant substrate, and the ADP-ribose remains on its normal target proteins leading to poor virus replication.